

Leo II: a distant dwarf spheroidal galaxy

Tim Olsson

Lund Observatory
Lund University



2017-EXA127

Degree project of 60 higher education credits (for a degree of Master)
June 2017

Supervisor: Sofia Feltzing

Lund Observatory
Box 43
SE-221 00 Lund
Sweden

Leo II:
a distant dwarf spheroidal galaxy

Master's thesis

Tim Olsson

Supervisor: Professor Sofia Feltzing

Lund Observatory

May 2017

Abstract

In this project aperture photometry has been performed for stars in the direction of the dwarf spheroidal galaxy Leo II. The observations were carried out using the Strömgren filters v , b and y , during three consecutive nights in 2003, out of which all but the first one turned out to be non-photometric. The data was reduced and calibrated (using the metallicity calibration of Calamida et al. (2007)) to yield magnitudes and metallicities for in total 2364 stars. Errors were estimated by means of Monte Carlo simulations. 152 stars correlate with stars observed in spectroscopic surveys, and are confirmed members of Leo II based on their radial velocity. We find an asymmetric metallicity distribution function, which extends towards lower metallicities, peaks at $[\text{Fe}/\text{H}] = -2.4$ dex, and has a spread of 1 dex. We also find signs of metallicity-dependent substructure within the galaxy, and a radial metallicity gradient of -0.220 ± 0.016 dex/ r_c . We generally find fainter magnitudes and lower metallicities for the stars in the galaxy than previous studies have done.

Populärvetenskaplig sammanfattning

Vi bor i Vintergatan, en av Universums många galaxer. Men hur bildades den, och alla andra galaxer vi kan se genom våra teleskop? Rådande teorier hävdar att för många miljarder år sedan, när Universum var ungt, bildades först små dvärggalaxer, som sedan slogs ihop till att bilda stora galaxer såsom Vintergatan. Men många detaljer i den här processen är fortfarande oklara. Därför vill vi titta på stjärnorna i de dvärggalaxer som finns kvar idag, och jämföra med stjärnorna vi ser omkring oss i vår egen galax, för att få ledtrådar till vad som hänt genom galaxernas historia.

En sådan dvärggalax är Leo II. Observationer av stjärnorna i denna galax gjordes under tre nätter i februari–mars 2003. I det här projektet har dessa data analyserats i hopp om att karaktärisera stjärnorna i Leo II. Den metod som använts i observationerna kallas för Strömgrenfotometri. Under fotometri placeras ett antal filter (ett i taget) som släpper igenom ljus av olika färg framför teleskopets detektor. Genom att räkna hur mycket ljus som kommer från en stjärna i varje given färg går det att bestämma t.ex. stjärnans temperatur och vad den består av. Om detta görs för många stjärnor i en galax kan det i sin tur ge indikationer om hur galaxens historia har sett ut.

Under analysen blev det uppenbart att under två av observationsnätterna hade vädret varit för dåligt för att datan skulle vara användbar. Alla resultat i den här studien är därför baserade på observationer från enbart en natt, vilket innebär att de inte kommer att vara lika statistiskt säkra som de annars hade kunnat vara. Vi får ändå fram mätvärden för totalt 2364 stjärnor.

Vi konstaterar att stjärnorna i Leo II tycks vara mycket metallfattiga ('metaller' betyder inom astronomin alla grundämnen förutom väte och helium), och att även de yngsta tycks vara minst 6 miljarder år gamla. Fördelningen av stjärnor och deras metallhalter tycks inte vara uniform över galaxens yta, utan där tycks finnas en trend där metallrikare stjärnor finns närmre galaxens centrum. Detta skulle kunna betyda att stjärnbildningen längst ut mot galaxens kanter slutade för mycket länge sedan, medan stjärnor fortsatte att bildas i en eller flera omgångar närmre dess centrum.

Genom enbart våra observationer kan vi inte vara säkra på vilka av stjärnorna vi har observerat som tillhör Leo II, och vilka som är förgrundsstjärnor som tillhör Vintergatan. Därför har vi jämfört våra resultat med andra studier som har kunnat mäta huruvida stjärnorna tillhör dvärggalaxen, och hittar 152 stjärnor bland våra som säkert tillhör Leo II. När vi jämför våra mätvärden med tidigare studier konstaterar vi att våra resultat ger konsekvent ljussvagare och metallfattigare stjärnor. Därför rekommenderar vi en uppföljningsstudie som tittar närmre på metallbestämningen.

Contents

1	Introduction	1
1.1	Dwarf spheroidal galaxies	1
1.2	Photometry	6
1.3	The colour-magnitude diagram	9
1.4	Leo II	13
2	Data and analysis	15
2.1	The observations	15
2.2	Data reduction	18
2.3	Detection of stars	18
2.4	Photometry	20
2.5	Photometric calibration	22
2.6	CMD and metallicities	28
2.7	Error estimation	29
2.8	Comparing nights	32
3	Results	38
3.1	Colour-magnitude diagrams	38
3.2	Metallicity	38
3.3	Membership determination	44
3.4	Age determination	46
3.5	Morphology	47
4	Discussion	49
4.1	Literature comparisons: photometry	49
4.2	Literature comparisons: spectroscopy	49
5	Summary	56
A	Tables	62
B	Plots	67

Chapter 1

Introduction

This project aims to characterise the stars in the dwarf spheroidal (dSph) galaxy Leo II in terms of metallicity, colour and age. Through photometric observations these parameters are determined, in the hope of producing data useful in galactic research. By studying dSph galaxies in detail and comparing their stars to those within our Galaxy we can obtain clues about galaxy formation and evolution.

1.1 Dwarf spheroidal galaxies

Throughout most of the history of humankind, our entire Universe was believed to be confined within the Milky Way. Everything we were able to observe via eye or telescope; planets, stars, stellar clusters and nebulae, was thought to be part of our home galaxy. It was not until the beginning of the 20th century that arguments were put forth for a world-view in which among others the great nebula in Andromeda (as it was known back then), were in fact galaxies of their own, residing at distances unfathomable compared with what had previously been imagined. In 1924 Edwin Hubble was able to establish its distance, through observations of cepheid variable stars¹ in the Andromeda nebula (Hubble 1925). It was thus confirmed that the object was indeed a galaxy of its own, of a size comparable to that of the Milky Way, situated over two million light-years away from even the furthest fringes of our galaxy.

Since then it has become apparent that our Milky Way is only one of many

¹These are stars of known brightness, also known as standard candles. Since they are recognisable through their periodicity, and the way intensity of light decreases with distance is known, astronomers can use them for distance determinations by measuring how faint they appear to be.

billions of galaxies, spread throughout an ever faster-expanding Universe (Riess et al. 1998). And although observations and simulations have taught us much, the formation of these worlds of stars, dust, gas and dark matter remains a relevant field of study in astrophysics even today.

A model of galaxy formation was put forth by Searle & Zinn (1978) which explained the halo of the Milky Way to have been formed through gradual merging of smaller systems; a hierarchical assembly. In our current Λ -CDM model of the Universe (Cold Dark Matter Universe dominated by dark energy) this scenario retains its validity (e.g. Peebles & Yu 1970). The Λ -CDM model predicts a Universe where initially small density fluctuations grow into structures via amplification by gravitation. This means that small halos of dark matter and stars, e.g. in the form of dwarf galaxies, are thought to first have formed separately and then merged into larger ones.

Therefore, in order to understand the formation and evolution of galaxies it is helpful to study the surroundings from which they formed. The immediate neighbourhood of the Milky Way is known as the Local Group. It is dominated by two large spiral galaxies: Andromeda and the Milky Way, along with a smaller spiral galaxy called Triangulum. Most of the Local Group's galaxies, however, are dwarf galaxies. They are significantly smaller and fainter than their larger counterparts, and thus far about 50 dwarf galaxies have been discovered in orbit around the dominant galaxies (e.g. Koposov et al. 2015).

Dwarf galaxies come in three types, distinguished by their morphology:

Dwarf irregular galaxies lack any clear structure or distinct features. They typically contain a lot of gas and often show signs of ongoing star formation (Grebel 2004). Two examples of dwarf irregular galaxies are the Large and Small Magellanic Clouds, which can be observed with the naked eye from the Earth's southern hemisphere.

Dwarf elliptical galaxies, on the other hand, contain very little gas, or none at all. Since gas is what stars are made from, this means that no star formation is expected to occur within them at present, and very little is indeed observed (e.g. Koleva et al. 2009). Apart from their elliptical shape, these dwarf galaxies are characterised by low surface-brightness and a distinct nucleus. An example of a dwarf elliptical galaxy which can be observed with a small telescope or binoculars is M32, which lies in orbit around the Andromeda galaxy.

Dwarf spheroidal galaxies are the faintest of them all. They have spherical or elliptical morphologies, very low luminosities, and in contrast to dwarf ellipticals display no nuclei. They are almost completely devoid of gas, and most of their stellar populations are very old. Compared with other dwarf

galaxies their luminosity is low, and they display very metal-poor stellar populations (Mateo 1998).

Common properties of all dSph galaxies include total luminosities of $M_B > -14$, while being fainter than $22 M_V \text{ arcsec}^{-2}$ due to the low density of stars. Their disk scale lengths vary between 100-400 pc (Gallagher & Wyse 1994), making them larger than globular clusters, whose disk scale lengths are typically smaller than 30 pc (van den Bergh 2008). Their projected axial ratios range between $0 \leq (1-b/a) \leq 0.6$ (Caldwell et al. 1992), meaning they all appear flattened. It was previously hypothesised that all dSph galaxies share a common mass profile (Strigari et al. 2008), but recent observations have practically disproven this claim (e.g. Collins et al. (2014)).

Dwarf galaxies remain an interesting topic of study, because while the hierarchical model works well for explaining the overall buildup of the Galactic halo, there are still many details in its formation scenario which remain to be filled in. There are several discrepancies between predictions and observations of the Λ -CDM model on small scales. For example, the model predicts more dwarf galaxy satellites around the Milky Way than have currently been observed.

This problem, known as the missing satellite problem, was alleviated somewhat when several new ultra-faint dSph galaxies were discovered in the Sloan Digital Sky Survey (SDSS, see e.g. York et al. 2000). There still seems to be about a factor of 4 missing, though, and it is unclear whether this is due to an inherent error in the theory or an observational bias (Simon & Geha 2007). One possible solution to the problem could be that low-mass dark matter halos formed before the reionisation of the Universe, and then had photoionisation feedback suppressing star formation below observable levels in up to 90 % of the cases in the Local Group (Ricotti & Gnedin 2005). This would mean that many missing satellites remain undiscovered because they have formed very few or no stars (Brown et al. 2013).

From the discussion above it is evident that dark matter is a field of study of great importance for galaxy formation, where observations of dSph galaxies are of great value. The virial theorem states that a relaxed system of gravitationally interacting particles will have a velocity dispersion (σ) related to the total mass of the system (M) through $\sigma^2 \propto GM/R$. If one then assumes that mass follows light, observations indicate that the stars of dSph galaxies should have central velocity dispersions $\leq 2 \text{ kms}^{-1}$. The actual velocity dispersion measured is however $\geq 7 \text{ kms}^{-1}$ for all dSph galaxies (Mateo 1998). This implies that the dSphs must contain a lot of dark matter. With mass-to-light ratios of around $150 M_\odot/L_\odot$ (Salvadori et al. 2008) they are in fact the most dark-matter-dominated systems known in the Universe

(compare with a M/L of $\sim 70 M_{\odot}/L_{\odot}$ for the Milky Way, Faber & Gallagher 1979).

This means that observations of the dynamics of dSph galaxies can be used for putting constraints on the nature of dark matter. Findings so far indicate that more luminous dSph galaxies contain more dark matter, and that they also contain fractionally larger amounts of metal². Furthermore, heavier dSph galaxies appear to have a relatively higher fraction of dark matter (Revaz et al. 2009).

The study of dSph galaxies can also help in the quest for knowledge about the earliest history of the Universe. Just after the Big Bang the Universe contained mainly ions of hydrogen (H). The free electrons had radiation scattered off of them, which made space opaque. After circa 300000 years the Universe cooled enough for the H to combine into atoms, making it so that light could pass through the now see-through universe. At around 1 Gyr after the Big Bang, over a relatively short period of circa 100 Myr, light from either many dim galaxies or quasars reionised the H. However, expansion had now made the density of the Universe low enough for space to be mostly transparent anyway, allowing light from this epoch to reach us across the years.

In most dSph galaxies the bulk of the stars are ancient (10 Gyrs or older, Salvadori et al. 2008). There is evidence of some dSphs having formed stars as recently as 3 Gyrs ago, but due to their lack of gas none are thought to be capable of star formation today (Gallagher & Wyse 1994). Furthermore, every dSph galaxy has been observed to contain a population older than 13 Gyr (Salvadori et al. 2008), and they are thus relics from the reionisation period of the Universe. This means that the chemical composition of these stars reflects the conditions at the very beginning of the star-forming era of the Universe.

dSph galaxies are the only well-defined samples for which we can derive complete star formation histories (SFHs). This is because they are well-isolated and their stars have not spread out since they were first formed, so through determination of the main sequence turn-off point (see §1.3) the ages of their populations can be unambiguously determined (Mateo 1998).

In order to derive the SFHs of the dSph galaxies, their chemical composition must be studied. Spreads in metallicity of up to 0.5 dex indicate that in contrast to globular clusters the star formation in dSph galaxies typically happens in several bursts, resulting in several populations of different ages (Simon & Geha 2007). Furthermore, there is a correlation between luminosity and metallicity, where more luminous dSph galaxies are on average more

²In astronomy, metals refer to all elements heavier than hydrogen and helium.

metal-rich (Caldwell et al. 1992). It has also been found that dSph galaxies have low abundances of α -elements (Harbeck et al. 2001).

α -elements (such as O, Mg, Si, Ca) are primarily produced in type two supernovae (SNe II), while iron-peak elements (such as Fe, Ni, Co) are produced in supernovae type Ia (SNe Ia). SNe II is the result of the death of massive stars, while SNe Ia occur in binary systems where one of the stars is a white dwarf. Since the early Universe was dominated by massive stars which would not evolve into white dwarfs, it is likely that only SNe II were able to enrich the primordial interstellar medium (ISM) before the globular clusters and dSphs formed. This would mean an enrichment of the ISM with both Fe and α -elements, resulting in relatively high $[\alpha/\text{Fe}]^3$. Objects that formed later, after SNe Ia had had time to enrich the ISM with more Fe, would then in contrast have lower relative α -element abundances. Subsequently, a decline of $[\alpha/\text{Fe}]$ is interpreted as a contribution by SNe Ia, and implies that an early termination of star formation did not occur (Salvadori et al. 2008).

The relative elemental abundances between dSph galaxies are also of interest. For example, if an isolated dSph galaxy was shown to have the same abundance pattern as the relatively nearby dSphs, this would indicate two things. First, that the lack of halo stars with dSph-like abundance patterns suggests that the vast majority of the Galaxy's halo formed very quickly and that dSph galaxies have contributed very few stars since. Secondly, that α -element deficits would not be an effect of dynamical stirring but are rather entirely due to dSph stellar and chemical evolution (Shetrone et al. 2009).

Before SDSS, nine dSph galaxies had been discovered (Mateo 1998). These are referred to as the classical dSphs, while the fourteen subsequently discovered are labeled ultra-faint (see Willman (2010) and references therein). Ultra-faint dSph galaxies are characterised by being very metal-poor. They all show similar colour-magnitude diagrams (CMDs, see §1.3), which indicates that their SFHs are synced to within about 1 Gyr (Brown et al. 2013). It is very unlikely that a coincidence such as this would be caused by stochastic mechanisms, such as gas depletion or supernova feedback, terminating the star formation within the individual galaxies. Rather there would appear to be a global phenomenon at work, such as re-ionisation dampening the star formation.

While much progress has been made recently both in simulations and observations of dSph galaxies, many details are still left to fill in, and several questions remain unanswered. Why, for example, are their fractions of dark matter so high? Which processes were responsible for stripping them of their gas? And how do environmental factors such as orbits around their host

³Notation explained in § 1.2

galaxies correlate with internal properties? The aim of this project is to help shed light on these and other questions by means of providing photometric data of stars in one dSph galaxy, with the ultimate hope of furthering our understanding of galaxy formation and evolution.

1.2 Photometry

A lot can be learned from investigating the spectrum of light emitted by a star. Starlight is comprised of photons of a range of different colours (i.e. wavelengths); from the low-energy infrared (IR) to the high-energy ultraviolet (UV). The relative amount of light emitted in each wavelength depends on a range of stellar characteristics, and so the spectrum of light holds the key to a number of parameters of a star.

In essence, a star behaves closely to a blackbody radiator, and so its intensity-distribution of light across a range of wavelengths depends upon its temperature according to Planck's law:

$$I(\lambda, T) = \frac{2hc^2}{\lambda^5} \frac{1}{e^{\frac{hc}{\lambda k_B T}} - 1},$$

where λ is the wavelength, T is the temperature, h is Planck's constant, c is the speed of light, and k_B is Boltzmann's constant. This gives rise to a radiation curve (see Fig. 1.1). From the figure it is clear that the maximum of the curve shifts redwards with decreasing temperature; blue stars are hotter than red ones.

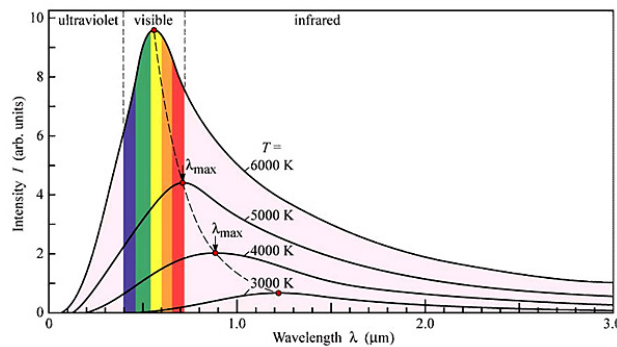


Figure 1.1 Black-body radiation at different temperatures; so-called Planck curves. Image source: Wikimedia Commons

Stars are not perfect black bodies, however. In their atmospheres are distributed atoms and ions of various elements that absorb and re-emit the

light which makes its way out from the stellar interior. Even though the light originally travels perpendicularly away from the surface of the star, the re-emission of a photon absorbed by an atom in its atmosphere occurs in a random direction. This results in less light overall traveling along a particular line of sight for the specific wavelengths corresponding to the energy-levels of the excitable electrons in the elements present, and so this will manifest itself in the form of dents, or lines, in the spectrum. The more atoms of a certain element, the more light will be scattered, meaning that the depth, or strength, of a line is proportional to the abundance of its corresponding element.

The detailed study of stellar spectra, known as spectroscopy, can thus gain us insight not only into their surface temperatures, but also into the chemical compositions of the stellar atmospheres and their elemental abundances. A disadvantage of spectroscopy is however that due to its many small wavelength bins, large amounts of light are required in order for the level of the signal to be significantly above the noise. This makes it difficult, to perform spectroscopy on apparently faint objects, such as dSph galaxies.

This is why the method *photometry* is a good alternative in these studies. Instead of investigating each wavelength in sub-nanometric detail, the principle of photometry is to have a few relatively broad ranges of wavelength within which to collect light. This is accomplished by utilising filters which are transparent to light within a certain range of wavelengths, but otherwise opaque. These are put (one at a time) in the way of the light collected by the telescope, and then it is simply a matter of counting the amount of photons which passed through each filter. By choosing the width and placement of the wavelength range for which the filters should be transparent carefully, the amount of light gathered within them can, if not yield a detailed abundance analysis, give insight into large-scale characteristics of the stellar spectra.

Today there exist a number of different photometric systems. The one used in this work is the system of Strömberg (1963), which utilises the four filters *u*, *v*, *b* and *y* (see Fig. 1.2).

- The *y* (yellow) filter is centred at 550 nm, has a full width at half-maximum of 20 nm, and is calibrated such that the *y* magnitude corresponds to the *V* magnitude of the Johnson photometric system.
- The *b* (blue) filter is centred at 470 nm with a full width at half-maximum of 10 nm. It thus encompasses the $H\beta$ absorption line, but stays clear of any other strong absorption lines.
- The *v* (violet) filter is centred at 410 nm and has a full width at half-maximum of 20 nm. It is thus centred at on $H\delta$, and encompasses many

other absorption lines. Because the presence of metals in a star give rise to absorption lines, this means that the v filter is very metallicity-sensitive.

- The u (UV) filter is centred at 350 nm and has a full width at half-maximum of 38 nm. This places its location bluewards of the Balmer jump, so in combination with the v filter the location of this discontinuity can be measured. The u filter is also metallicity-sensitive because it is affected by line blanketing (reduction of light because of many absorption lines) to a degree of about twice as much as the v filter.

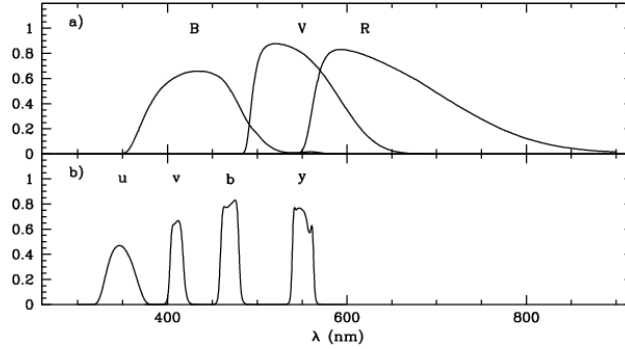


Figure 1.2 Throughput as a function of wavelength for each filter in a) the conventional Johnson photometric system, and b) the Strömgren photometric system. Figure from Árnadóttir et al. (2010).

From these four filters a number of photometric indices can be constructed. $(b - y)$ or $(v - y)$ measures the steepness of the stellar spectral energy distribution, and therefore indicates colour and thus temperature. The higher the value of a star in these indices, the redder and cooler it is. This is, however, not unambiguous, since (as we shall see) the metal content also affects the colour of a star.

Furthermore, there are the m_1 and c_1 indices:

$$m_1 = (v - b) - (b - y)$$

$$c_1 = (u - v) - (v - b).$$

Because the m_1 index measures how much v differs from the colour gradient $(b - y)$ it measures the effect of absorption lines diminishing the light of a star (the so-called blanketing effect), and thus allows for determinations of metallicity to good accuracy. Since iron (Fe) is the most abundant metal, its

abundance is often taken to represent the overall metallicity of a star, and is defined as follows:

$$[\text{Fe}/\text{H}] = \log_{10} \left(\frac{N_{\text{Fe}}}{N_{\text{H}}} \right)_* - \log_{10} \left(\frac{N_{\text{Fe}}}{N_{\text{H}}} \right)_{\odot}$$

where N represents the number of atoms per unit of volume, $*$ represents the star, and \odot represents the Sun. It is thus a logarithmic quantity normalised against the Sun.

The c_1 index measures the strength of the Balmer jump, and is thus sensitive to luminosity. Because this index measures how much b differs from the colour gradient ($v - b$), and because the blanketing in b is about twice that in v , it is not metallicity-sensitive. Therefore it can be used to separate dwarfs from giants without getting stuck in a metallicity-luminosity degeneracy (Adén et al. 2009). This tends to be a problem otherwise, because low luminosity could in itself either be caused by the star having a small surface area, or blanketing from many absorption lines.

In summary, the Strömrgren photometric system is advantageous to use mainly because metallicity measurements can be performed for a large number of stars simultaneously, without the need for medium-resolution spectroscopy. A drawback is however that because the filters are fairly narrow, the exposure times needed in order to collect enough light can be very long for faint targets (around 20 minutes or more), leading to great sensitivity to observational circumstances.

1.3 The colour-magnitude diagram

There are two parameters which are of chief interest when studying stellar populations: luminosity and temperature. In photometry these physical characteristics are represented by magnitude and colour, respectively. Magnitude is a measure of the intensity of a star's light in a certain filter, and is defined as follows:

$$m_i = m_{\text{ref}} - 2.5 \log_{10} \left(\frac{I_i}{I_{\text{ref}}} \right)$$

where i is the filter in question, m_{ref} is a reference magnitude which depends on the calibration of the photometric system used, I_i is the intensity of the star, and I_{ref} is the intensity of the star used for reference. Note that this definition results in a higher luminosity corresponding to a lower magnitude. A common notation for the magnitude in a certain filter is simply i , i.e. u , v , b , and y in Strömrgren photometry.

A distinction is also made between apparent and absolute magnitude, where apparent refers to the magnitude as measured from Earth (though corrected for extinction), while absolute refers to the magnitude which would be measured if the star was placed at a distance of 10 parsecs (pc). Stars visible to the naked eye have apparent magnitudes ranging between circa -1 and 6, while the very largest telescopes can distinguish objects of magnitude 25 or higher.

Plotting magnitude against colour in a so-called colour-magnitude diagram (CMD, also known as a Hertzsprung-Russel or HR diagram) can reveal a wealth of information about a group of stars. An example of a CMD is shown in Fig. 1.3.

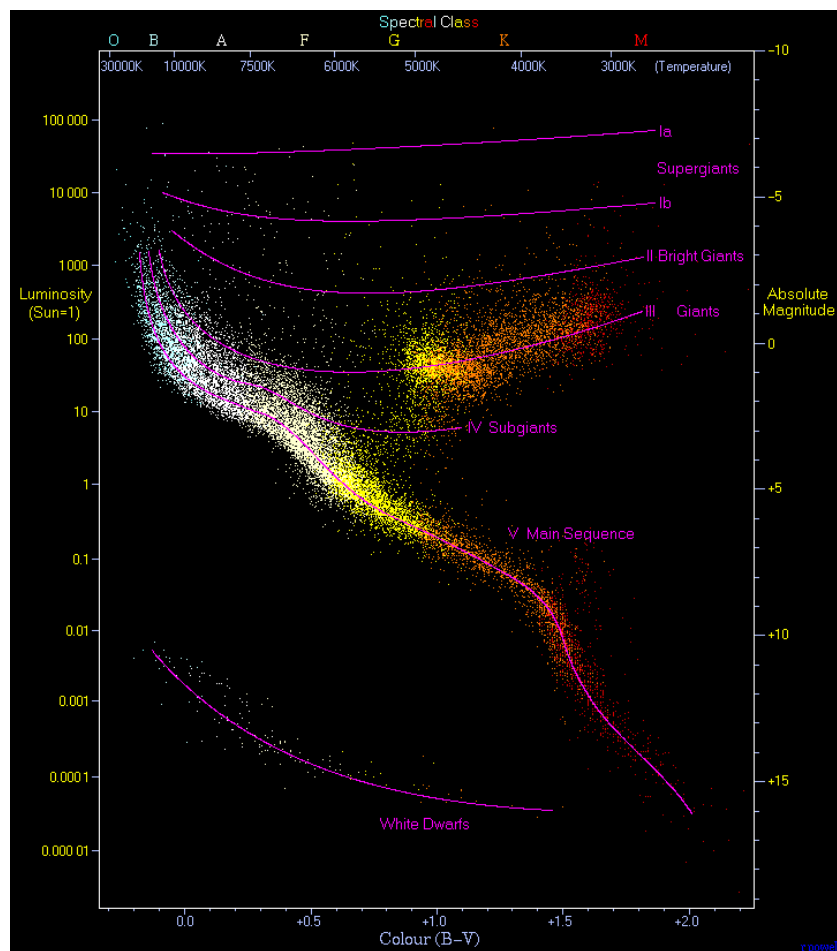


Figure 1.3 Colour-magnitude diagram featuring 22000 nearby stars from the Hipparcos catalogue and 1000 stars from the Gliese catalogue. Image source: Wikimedia Commons

A prominent feature of the CMD is the fact that stars, rather than being scattered all over the place, cluster in certain areas. The biggest such group is the so-called main sequence, which runs diagonally from the upper left corner of the diagram to the bottom right. This is where stars spend most of their existence after their ignition, converting hydrogen into helium (He) via fusion. A star's position on the main sequence is determined by its initial mass; the heavier the star, the brighter its luminosity will be, and the hotter its temperature will be. In terms of magnitude and colour this means that the heaviest stars will have a low magnitude and a low colour index, placing them at the upper left end of the main sequence. Correspondingly, the lightest stars will shine dimly and at a red colour, placing them at the lower right end of the main sequence. All main sequence stars are commonly referred to as dwarf stars.

Stellar evolution⁴ will move a star further up and to the right in the CMD, following a path referred to as the red giant branch (RGB). When a star reaches this stage its luminosity increases up to a factor of 1000. This means that RGB stars, being so bright, are usually the main target when observing distant populations such as dSph galaxies.

When the so-called helium flash occurs, the star will become bluer while roughly maintaining its luminosity, placing it along the horizontal branch (HB) once it has settled in its new equilibrium. Further evolution will cause the star to cool and expand once more, moving it upwards and to the right along the asymptotic giant branch (AGB). The time spent on the RGB, HB and AGB by a star is considerably shorter than its time on the MS; on the order of Myrs rather than Gyrs.

This evolutionary process leads to every star following its own unique path in the CMD, where it starts off on the main sequence and subsequently moves onto the RGB, HB, and AGB⁵. The starting position and time at which it leaves the main sequence, i.e. its turn-off age, depends in part on its initial mass, but also on its metallicity. Increased metallicity affects the lifetime of a star by increasing its opacity. Greater opacity leads to a higher temperature, which in turn leads to the star burning its fuel faster and so hastens its evolution. This means that the star would move off the main sequence earlier than a star of equal mass but with lower metallicity would do.

Increased metallicity also affects the stars' spectra in the form of spectral lines. Especially Iron absorbs more light in the blue part of the spectrum

⁴For details on the stellar evolutionary process, see e.g. Prialnik (2000).

⁵Except for stars heavier than $8M_{\odot}$, which evolve differently. These stars are, however, exceedingly rare, and will not be discussed further in this work.

than in the red, which leads to a so-called line blanketing effect through which the stars appear redder than they would otherwise be because of the many absorption lines diminishing the amount of blue light.

Determining the age of a single star is difficult, because if for example it is found along the MS, it is not evident for how long it has been there. This is why it is advantageous to study whole populations of stars. One interesting thing to look at then is the colour beyond which there are no bluer stars. This colour, known as the turn-off colour, will move red-wards with time, since the stars which are initially bluest (i.e. hottest) evolve off the main sequence most quickly. By finding this colour an idea can be made about what stars have had the time to evolve onto the RGB, and thus yield an indication of the age of the population⁶. However, because a high metallicity will affect the location of the main sequence turn-off (MSTO) by moving it red-wards, metallicity needs to be determined separately in order to break this degeneracy.

A useful tool when studying stellar populations (such as dSph galaxies) are isochrones. If one plots stars of all masses in a CMD at a certain point in time, one will obtain a curve where the MSTO is clearly visible. An example of isochrones is shown in Fig. 1.4. Comparing the metal-rich with the metal-poor makes it evident that the metallicity of the population must be known before a good fit can be made. An isochrone is strictly speaking a theoretical construction, based on models of star formation and stellar evolution. Simulated isochrones are calibrated against observational data, making them (as used in this work) a semi-empirical entity.

Because dSph galaxies are faint and distant, mostly giant stars will be available for observation. This means that instead of using isochrones to fit the MSTO, we will use them for fitting the RGB. Also in this case it is important to keep in mind the age-metallicity degeneracy, but because Strömgren photometry can provide metallicity determination there is no need to rely on spectroscopy for this purpose.

⁶Note, however, that if multiple populations are studied within the same sample, only the youngest will be identified through this method.

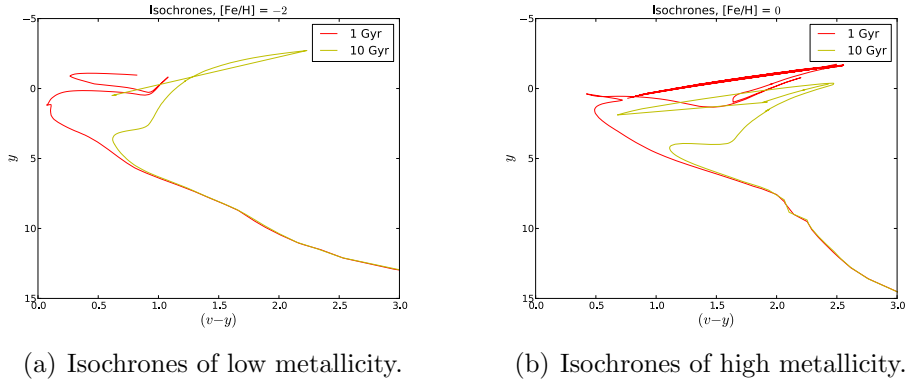


Figure 1.4 Isochrones of ages 1 and 10 Gyr for stars of (a) low ($[\text{Fe}/\text{H}] = -2$) metallicity, and (b) high (solar) metallicity. Source: PADOVA online database (Marigo et al. 2017).

1.4 Leo II

Leo II is one of the classical dSph galaxies, discovered by Harrington & Wilson 1950. Located in the constellation of Leo, its coordinates on the sky are R.A. = $11^{\text{h}} 13^{\text{m}} 28^{\text{s}}.8$, Decl. = $+22^{\circ} 09' 06''$ (epoch J2000). In galactic coordinates this translates to $l = 220^{\circ}$, $b = 67^{\circ}$, meaning it is located well above the disk of the Milky Way, in a direction away from the Galactic centre. This means that its line of sight is relatively unobstructed by stars belonging to the Milky Way, and also that the reddening of light due to interstellar dust is negligible (Schlafly & Finkbeiner 2011). There is, however, a metal-poor debris stream from the Sagittarius dSph galaxy passing in front of it.

Leo II lies at a distance of 233 kpc, as measured by Bellazzini et al. (2005) by means of the observed luminosity of the tip of the RGB. This is a large distance, and so it has been questioned whether Leo II is gravitationally bound to the Milky Way or not (e.g. Demers & Harris 1983). Its radial velocity of 26.2 km s^{-1} (Siegel & Majewski 2000) and dSph morphology indicate it is reasonable to consider it a Milky Way satellite (McConnachie 2012). However, taking into account its lack of evidence for tidal disruption (Koch et al. 2007), there remains the possibility that the galaxy evolved in isolation within the Local Group and is only now approaching the Milky Way for the first time.

Over the years several photometric studies have targeted Leo II, resulting in measurements of in total several thousand stars. From these surveys it has been concluded that the mean age of the stars in Leo II is circa 9 Gyr, and that there has been little to no star formation going on in the galaxy during

the last ~ 7 Gyr (Mighell & Rich 1996). Photometric studies have also found that red clump stars (i.e. red HB stars) are more centrally concentrated than blue HB stars (Bellazzini et al. 2005); that a mixture of stellar populations exists in the galaxy’s centre, while an older, more homogeneous population extends to larger radii (Komiyama et al. 2007).

One advantage of using spectroscopy rather than photometry is the possibility of determining the radial velocity of the stars based on the doppler shifts of the absorption lines in their spectra. This, in turn, can be used to determine whether or not the stars are members of the galaxy by checking whether they fall within the galaxy’s systemic velocity dispersion. However, because the galaxy’s large distance presents difficulties, far fewer stars have been observed spectroscopically than photometrically.

One spectroscopic study was performed by Koch et al. (2007), in which 195 stars were observed. 52 of these were concluded to be members based on their velocity measurements falling within the systemic velocity of 79.1 ± 0.6 km s⁻¹, with dispersion 6.6 ± 0.7 km s⁻¹, determined in the study. A metallicity range between $-2.4 < [\text{Fe}/\text{H}] < -1.08$ was found, with a peak at $[\text{Fe}/\text{H}] = -1.74$ dex, and a negligible radial metallicity gradient. Because they found no gradient or asymmetry in the velocity, nor any signs of rotation, they concluded that the galaxy had not been affected by tides.

Another spectroscopic study by Kirby et al. (2010) targeted 294 RGB stars, 258 out of which were determined to be members based on their radial velocities. In a follow-up study (Kirby et al. 2011) focused on chemical abundances they found a metallicity gradient of $d[\text{Fe}/\text{H}]/d(r/r_c) = -0.21 \pm 0.01$ dex, where $r_c = 180$ pc is the core radius (as determined by Irwin & Hatzidimitriou 1995).

A more recent spectroscopic survey was carried out by Spencer et al. (2017), where 175 out of 336 observed RGB stars were concluded to be members. According to this study, the systemic velocity of Leo II is 78.3 ± 0.6 km s⁻¹, with a dispersion of 7.4 ± 0.4 km s⁻¹; its mean metallicity -1.70 ± 0.02 dex; and its radial metallicity gradient -0.28 ± 0.1 dex/ r_c .

Because the Strömgren system allows for metallicity determination, it will be interesting to determine the peak and spread of Leo II’s metallicity distribution, look for gradients or structure in metallicity across the surface, and attempt age determination via isochrones; and to compare the results with previous studies. All with the ultimate goal to gain clues about the SFH of Leo II, and in the grander scheme of things expand the knowledge about dSph galaxies and their role in the formation of larger galaxies.

Chapter 2

Data and analysis

At the very moment that humans discovered the scale of the universe and found that their most unconstrained fancies were in fact dwarfed by the true dimensions of even the Milky Way Galaxy, they took steps that ensured that their descendants would be unable to see the stars at all.

— Carl Sagan (Contact)

2.1 The observations

dSph galaxies reside far outside the Milky Way, and because of this great distance the stars within them appear faint to us. Due to their low apparent brightness care must be taken in their observations in order to gather as many photons as possible, through which to characterise them. Distance is, however, not the only problem observers are faced with when performing these studies.

All Earthbound observations are sensitive to environmental conditions, including turbulence and moisture in the atmosphere, and light pollution. Therefore the ideal location for a telescope is a dry place with as little air turbulence as possible, far removed from the lights of civilisation. This is why the biggest observatories in the world are built on top of mountains, above the part of the atmosphere where most weather phenomena occur so that both turbulence and humidity is considerably lower than at sea level. And while in our modern times it is more or less impossible to find a place far enough from civilisation that the sky is completely dark and free of stray light, mountains often have the advantage of the light pollution being less severe.

One such place deemed fitting for observations is the Spanish island La Palma. Being one of the Canary islands, it is situated off the West coast of



Figure 2.1 (a) NOT and (b) ALFOSC, both featured together with the author. Photo credit: Dan Kiselman

Africa. Atop the island an old volcano rises 2.4 kilometres above sea-level. At such a height the otherwise subtropical climate is dry, and the winds from the west (cooled by the atlantic) provide good prerequisites for stable seeing¹. Furthermore, the island's isolation combined with severe restrictions regarding light emission on the island itself, makes its sky one among the Earth's darkest.

There, at the rim of the volcano, is situated the Observatoria del Roque de los Muchachos. It hosts 13 of the world's most advanced telescopes, among which is the Nordic Optical Telescope (NOT). Operational since 1989, the NOT is run by a consortium of Sweden, Denmark, Norway, Finland and Iceland. The telescope is a reflector with a primary mirror of 2.56 m diameter, which utilises active optics to prevent the mirror from deforming under its own weight. Its most-used instrument is the Andalusia Faint Object Spectrograph and Camera (ALFOSC). It consists of a 2048×2048 pixels charge-coupled device (CCD) with a field of view of size $6.4' \times 6.4'$ (an area corresponding to about $1/16^{\text{th}}$ of the full Moon). The telescope and camera are depicted in Fig. 2.1.

The big size of the telescope and the versatility of the camera make them suitable for observations of objects as faint as dSph galaxies, so the observations for this work were carried out at the NOT using the ALFOSC. The u filter was not utilised during the observations because the signal-to-noise ratio for most stars in that band would be exceedingly low for this faint target. Leo II was observed by Sofia Feltzing and Ingemar Lundström during 28 February–2 March 2003. During the first night the photometric conditions were fairly good. During the second and third nights, however, clouds made

¹Astronomical seeing refers to the effect through which stars appear blurred and twinkling when the refractory index of the atmosphere changes along the line of sight due to air turbulence.

for worse seeing and high extinction. The usefulness of the data obtained during these two nights is discussed in detail in § 2.8.

During the observations, not only the galaxies themselves were imaged. In order to calibrate the data for the galaxies correctly, additional information is needed. First of all, the dark current in the CCD has to be taken into account. This dark current consists of random noise within the detector, and may vary in time. Therefore, for every object observed, a so-called bias frame is taken with the shutter closed and at an exposure time of 0 seconds. Later on this will be subtracted from its corresponding image in order to make sure the zero-levels of the CCD counts are placed where they should be: at zero.

The sensitivity of a CCD can vary from pixel to pixel. Some pixels may be dead (yielding no counts), while others may be hot (erroneously yielding maximum counts), and whole areas of the CCD may be defect to some degree. Therefore so-called flat field images are taken of a uniformly bright area, in this case a relatively empty piece of sky at dusk and dawn. The pixel values recorded in the flat field are used later on to compensate for dust or other variations in the optical system as well as irregularities in the CCD.

A star or a galaxy will appear differently with respect to colour and intensity depending on its height above the horizon. This is because the light has to travel through a greater part of the Earth's atmosphere when an object is viewed close to the horizon than when it is high in the sky. Since more air particles will absorb and scatter especially blue light to a higher degree, greater airmass leads both to dimming and reddening of the light. In order to be able to correct for varying airmass a reference is needed whose magnitudes are previously known. For this purpose a number of so-called extinction stars are observed several times throughout the night. Since they are observed at different airmass, from this can be deduced an airmass correction factor for the science images.

When imaging stars in a distant galaxy through a telescope we would only obtain their apparent magnitude, unless we had a light-source of known intensity to compare them with. Therefore a number of so-called standard stars, of previously known apparent magnitudes, are observed throughout the night. In order to be able to compensate for potential variations in apparent magnitude depending on colour (e.g. through atmospheric effects), the standard stars have been chosen to span a wide range of colours. A list of the standard stars used in these observations is included in Table A.1.

2.2 Data reduction

The Image Reduction and Analysis Facility (IRAF²) software was used in the reduction and analysis of the observational data. Its packages were in this project accessed via Python scripts written by the author.

Firstly all images were inspected visually, and ones with obvious anomalies (such as the star being entirely gone from the field of view) were discarded from further analysis.

The standard stars were all subtracted by their respective bias frame using the IRAF package `IMRED`. Because these stars were imaged using only a small part of the CCD (known as windowing) it was not deemed necessary to further calibrate them using flatfields, and so they were subsequently considered ready for photometry.

The flatfields were bias-subtracted in the same manner as the standard stars and averaged using the IRAF function `flatcombine`, which is a part of the `CCD` package of `IMRED`. Flats from all nights were used for each filter separately, in order to create a so-called master flat for using on all science frames (i.e. the images of the dSph galaxy). The science frames were consecutively bias-subtracted and then multiplied with the normalised master flat of the corresponding filter. The following operation was thus performed (using the IRAF function `IMARITH`):

$$\langle \text{CALIB} \rangle_{X,Y} = \left(\frac{\langle \overline{\text{FLAT}} \rangle}{\langle \text{FLAT} \rangle_{X,Y}} \right) (\langle \text{RAW} \rangle_{X,Y} - \langle \text{BIAS} \rangle_{X,Y}),$$

where $\langle \text{CALIB} \rangle_{X,Y}$ is the calibrated image (X and Y referring to pixel coordinates), $\langle \overline{\text{FLAT}} \rangle$ is the average pixel value of the central part of the master flat, $\langle \text{FLAT} \rangle_{X,Y}$ is the master flat, $\langle \text{RAW} \rangle_{X,Y}$ is the uncalibrated image, and $\langle \text{BIAS} \rangle_{X,Y}$ is the corresponding bias (Berry & Burnell 2000).

Example of bias and flatfield frames are shown in Fig. 2.2.

2.3 Detection of stars

In order to be able to perform photometry on the stars their coordinates within the image must be known. Therefore the next step in the analysis is to create a procedure for detecting stars within the science frames. One of the sharpest images is chosen as a reference frame. Detection of stars is then

²IRAF is distributed by the National Optical Astronomy Observatories, which are operated by the association of Universities for research in Astronomy, Inc., under cooperative agreement with the National Science Foundation.

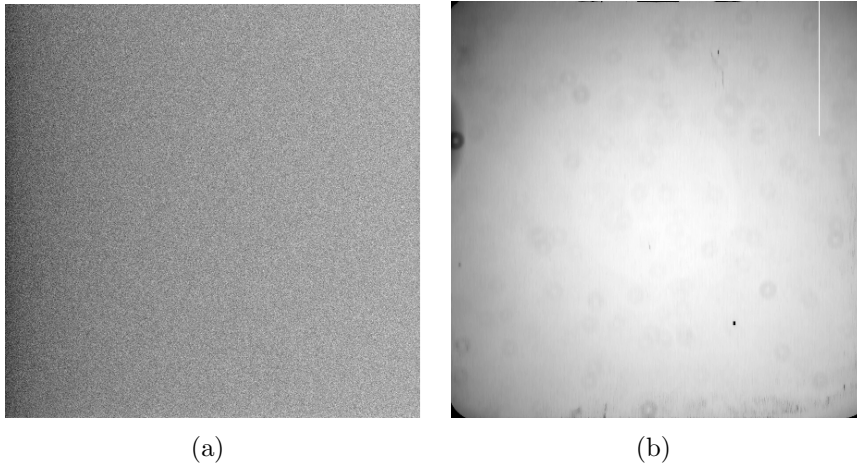


Figure 2.2 (a) Bias frame, in which the random noise of the CCD is depicted. (b) Flatfield frame, in which the pixel-to-pixel variations in the sensitivity of the CCD are depicted. Note features such as dead or hot pixels, brighter and darker areas, and circular shapes due to dust motes.

performed for this frame only, and their coordinates are subsequently used for all frames.

The resulting coordinate list is then shifted manually for the frames where the fields of view are not perfectly aligned with the reference frame. The shift is performed by visually inspecting the frames and noting how much they deviate from one another, and then translating the coordinates through adding or subtracting the corresponding number of pixels, using the function `LINTRAN`. This procedure is preferred rather than shifting the images themselves because (besides being simple) it keeps the same number of stars in the coordinate lists, and their identification numbers correspond directly to one another.

Each observed star will leave a signature on the CCD in the form of a point-spread function (PSF). The exact characteristics of the function depends on a variety of factors such as the telescope, the CCD, and atmospheric conditions, but in general it can be said that the higher the amplitude of the function, the brighter is the star observed. The algorithm used for star detection (by the IRAF function `DAOFIND`) requires an estimate of the shape of the stellar PSFs. Therefore the full width of the PSF at half its maximum (FWHM) is measured for a number of reasonably bright stars, and an approximate average is handed to `DAOPHOT` as a preset.

Since there will always remain a certain amount of background noise in the image there will be a certain amplitude below which the PSF will be

indistinguishable from the noise. Therefore the minimum pixel value of the background (i.e. between the stars in the galaxy) is investigated, along with its standard deviation (σ). In combination with the DAOFIND parameter *threshold* these quantities defines a lowest level in pixel counts below which faint objects will be treated as noise and thus not be detected.

The threshold parameter is defined in units of σ , and may vary between nights. To determine a suitable threshold value the DAOFIND algorithm is run several times on the reference frame while varying the threshold between 0.5 and 6.5 in steps of 0.5. The number of stars detected in each run is then counted and plotted against threshold level, as in Fig. 2.3. From the plot a threshold value should be chosen from just below where the curve begins to flatten out (in this example around 2.5σ). This in order to make sure most stars are detected without overcrowding the field with faint objects which might as well be noise.

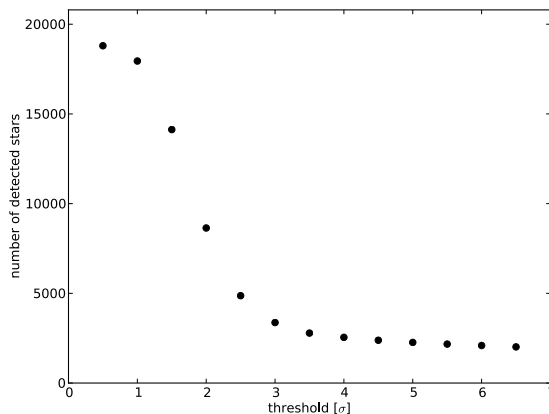


Figure 2.3 Number of stars detected in a frame as a function of the threshold (measured in units of standard deviation from the background noise, i.e. σ) for feature detection.

When all these parameters have been set to desired values, DAOPHOT is once again run on the reference frame, and a coordinate list is thus obtained.

2.4 Photometry

Photometry aims to measure the light collected from each star. In this work this is done via aperture photometry. The principle then is to choose an area within a certain radius of the centre of each PSF and measure all the light collected within that radius. A problem with this method is that in order

to make the aperture encompass the PSF in its entirety, there is likely to be measured flux contributed by tails of other overlapping PSFs, and noise, so that the resulting measurement would yield a brighter magnitude for the star than it actually possessed.

In order to solve the overlap problem an aperture considerably smaller than the full extent of the PSF is used. The measured flux is then multiplied by a correction factor in order to obtain the full flux of each star. The aperture correction factor may differ from frame to frame, and is therefore determined for each frame separately.

In order to find the aperture correction, circa 10 relatively bright and isolated stars are chosen. Aperture photometry is then performed on the stars using the function `PHOT`, with apertures of radii ranging from 2.5 to 40 pixels in steps of 2.5 pixels. The resulting fluxes are plotted for each star separately as in Fig. 2.4, a so-called curve of growth.

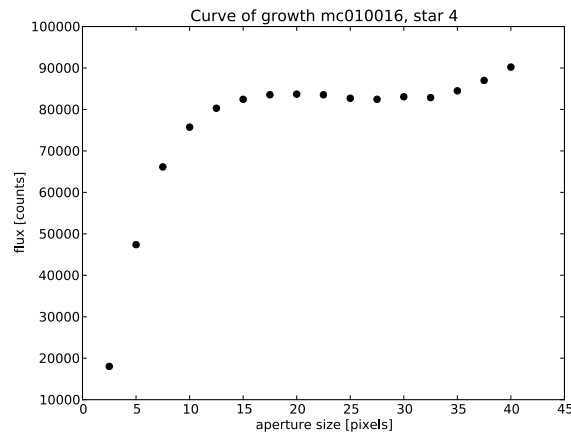


Figure 2.4 Flux for one star measured within apertures of increasing radii.

From the plots it becomes evident that at a certain aperture radius the curve of growth levels out (r_1), meaning that beyond this limit the PSF has decreased into the noise level and thus that flux outside this aperture needs not be taken into account. The actual aperture size (r_a) to be used for each frame is set to the same size as the FWHM of the PSFs. The aperture correction factor is then calculated from the ratio between the fluxes at these radii:

$$\frac{f_{r_1}}{f_{r_a}}$$

In order to correct for noise, the background sky around each star is also measured in an annulus around the aperture. The size of this should be

about three times the number of pixels contained within that of the source aperture (Howell 2000). The sky is then subtracted from the flux of the stars.

Finally, before photometry can be performed, two parameters specific for the CCD used must be specified in PHOT: gain and readnoise. Gain is measured in electrons per count, meaning the amount of electron charges corresponding to one flux count (0.736 for ALFOSC). Readnoise, measured in electrons, is the noise level of the CCD readout (5.3 for ALFOSC). When all parameters are set, PHOT is run on all frames.

2.5 Photometric calibration

During photometry the flux of the stars that have reached the CCD has been measured. However, because the amount of this flux depends on a number of factors affecting the observations, the stars need to be calibrated against stars of previously known magnitudes, i.e. standard stars. These are also observed throughout the night, and photometry is performed upon them in a similar fashion as upon the stars in the galaxy. However, since these stars are specifically chosen to be fairly isolated, and they are very bright, an aperture which encompasses the entire PSF is used, and so aperture corrections are not needed.

A few of the standard stars are so-called extinction stars. These have been observed several times throughout the night, at different elevations on the sky and thus their light has passed through different amounts of atmosphere for each observation. The amount of airmass is defined as $X = \sec \theta$, where θ is the angular distance of the star's position from zenith. The range in airmass of the extinction stars is used to find an extinction coefficient, k . Extrapolating to $X = 0$ would give the magnitude of the star observed outside the atmosphere, and so k is used to correct the photometry for atmospheric extinction.

The rest of the standard stars have been chosen to span as large a range of colours as possible. This is in order to be able to correct for possible systematic variations in e.g. the sensitivity of the CCD depending on colour, through a correction factor a . All of the standard stars are also used to find the zero-point, z , for each night's observations.

After having corrected the photometry for airmass and colour variation, there might still remain a dependence upon time of observation, because of changing atmospheric conditions throughout the night (e.g. clouds passing by). Therefore a correction factor α is introduced in order to account for the time of night of the exposure. Even though variations may occur over the course of a galaxy exposure (being 30 minutes long), the time of observation

is assumed to be that of the beginning of the exposure.

The final magnitudes of the observed stars obey the following calibration equation:

$$m_{s,i} = m_{0,i} + k_i X + a_i(m_v - m_y) + \alpha_i T + z_i, \quad (2.1)$$

where i denotes the filter (v , b or y in this study), m_s is the standard (catalogued) magnitude, m_0 is the raw observed magnitude, k is the extinction coefficient, X is the airmass, a is the colour coefficient, m_v and m_y are the standard magnitudes in v and y , α is the time coefficient, T is the time at the start of the exposure (in units of days according to the Julian calendar), and z is the zero-point. Because m_s , m_v and m_y are known for the standard stars (see Table A.1) this equation can be used to determine the values of k , a , α and z .

In order to find k , a , α and z , Eq. (2.1) is solved in a multi-step process. This is done separately for each filter, hence the lack of filter notation in the following equations. In step 1 extinction- and standard stars are used to find a first approximation of k and z . A linear regression is done with $m_s - m_0$ fitted against X :

$$m_s - m_0 = kX + z'$$

Colour and time are not corrected for in this step. Outliers deviating more than 5σ from the fit are removed, a process known as σ -clipping. An example of the fit is shown in Fig. 2.5.

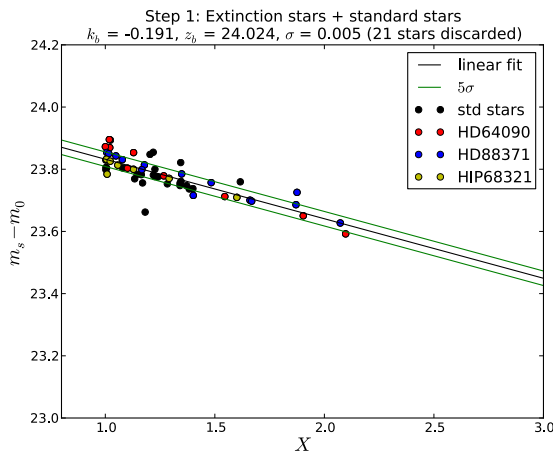


Figure 2.5 Deviation from standard magnitude of extinction stars depending on airmass. The green lines on either sides of the fit denote a 5σ deviation.

In step 2 the standard stars are used to find a first approximation of a . This is done via a linear regression with $m_s - (m_0 + kX + z')$, where k and

z' are the airmass constant and zero-point obtained in step 1, fitted against the catalogue colour $m_v - m_y$:

$$m_s - (m_0 + kX + z') = a(m_v - m_y) + z''$$

The stars removed in step 1 remain discarded, but no additional sigma clipping is performed in this step. An example of this fit is shown in Fig. 2.6.

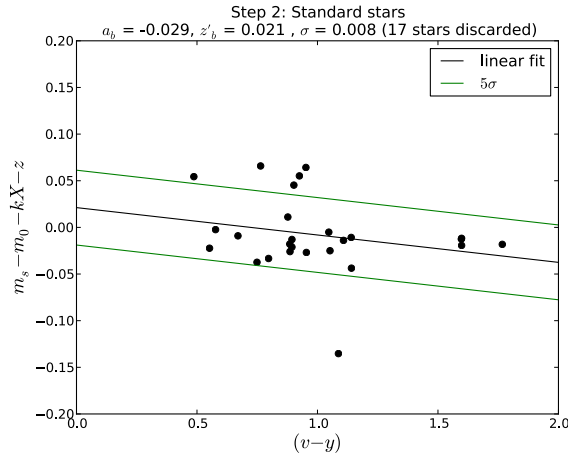


Figure 2.6 Deviation from standard magnitude of standard stars depending on colour. The green lines on either sides of the fit denote a 5σ deviation.

In step 3 the extinction stars are used to find a first approximation of α . A linear regression is done where $m_s - (m_0 + kX + a(m_v - m_y) + z' + z'')$ is fitted against T , k here being the extinction coefficient obtained in step 1, a the colour constant from step 2, and z' and z'' the zero-points of steps 1 and 2 respectively.

$$m_s - (m_0 + kX + a(m_v - m_y) + z' + z'') = \alpha T + z'''$$

The stars removed during step 1 remain discarded, and a clipping at 5σ is performed. An example of this fit is shown in Fig. 2.7.

In step 4 the process of step 1 is repeated, although now first correcting for both colour and time:

$$m_s - (m_0 + a(m_v - m_y) + \alpha T + z'' + z''') = kX + z',$$

where z'' and z''' are the zero-points from steps 2 and 3, respectively. Outliers are once again removed in a 5σ -clipping.

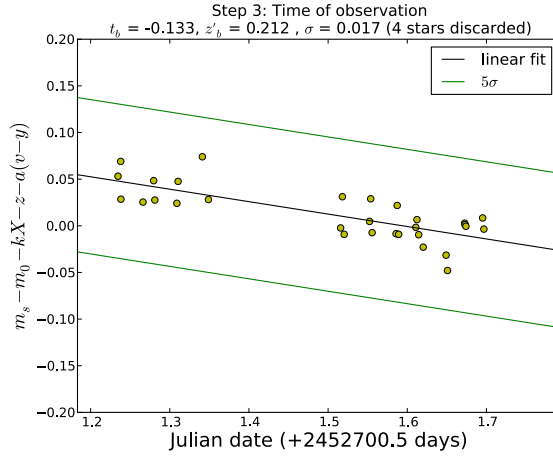


Figure 2.7 Deviation from standard magnitude of extinction stars depending on time of observation. The green lines on either sides of the fit denote a 5σ deviation.

In step 5 the process of step 2 is repeated, although this time correcting for both airmass and time:

$$m_s - (m_0 + kX + \alpha T + z' + z''') = a(m_v - m_y) + z'',$$

where k , α , z' and z''' are the coefficients and constants obtained in the two previous steps. An additional 5σ -clipping is performed.

In step 6 the process of step 3 is repeated, with the airmass and colour coefficients and constants from the two previous steps. A final 5σ -clipping is performed.

In step 7 the standard- and extinction stars are fitted one final time as in step 4, using the colour and time coefficients and constants from the two previous steps. Because k , a and α at this point have converged to within the third decimal, no further iterations are deemed necessary. The zero-points are combined from steps 5, 6 and 7 into one ($z = z' + z'' + z'''$).

The uncertainties of the calibration constants were calculated in the last three steps as the standard errors ($\hat{\sigma}$) of the slope and intercept of the line produced in the least-square fits. This is for $\hat{\sigma}_k$, $\hat{\sigma}_a$ and $\hat{\sigma}_\alpha$ done as follows:

$$\hat{\sigma} = \sqrt{\frac{SSE}{n-2}} \cdot \sqrt{\frac{1}{\sum (x_i - \bar{x})^2}},$$

where SSE is the sum of the squares of the residuals, n is the number of stars used in the fit, and x are the values fitted against for the stars in question

(i denoting one single measurement, and \bar{x} the average). $\hat{\sigma}_z$ is calculated as follows:

$$\hat{\sigma} = \sqrt{\frac{SSE}{n-2}} \cdot \sqrt{\frac{1}{n} + \frac{\bar{x}^2}{\sum (x_i - \bar{x})^2}}$$

Plots from all steps (examples of which are shown in Figs. 2.5 to 2.7) are inspected. Far-off outlier stars are inspected in order to determine whether their photometry appears to be good or if the star is de-focused, has an odd shape, etc., in which case it is removed from the sample and the process is started over.

To check the quality of the calibration the constants are applied to the photometry of the standard stars (according to Eq. (2.1)), and then the residuals compared with the catalogue magnitudes are plotted with respect to magnitude, colour, airmass and time of observation. An example of such a plot is shown in Fig. 2.8. If there is any systematic deviance (e.g. bad portions of the night can be discovered in this fashion) the stars considered unreliable are omitted and the iteration is redone. The final calibration constants and their respective uncertainties are listed in Table A.2. Final calibration plots for extinction- and standard stars, along with residual plots for each filter, are shown in Figs. B.1 to B.4 in Appendix B.

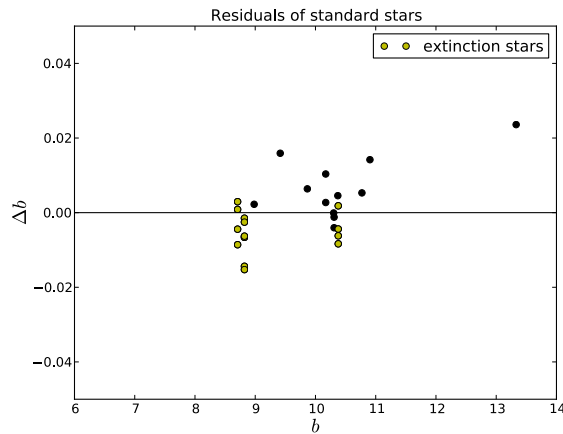


Figure 2.8 Residuals after calibration of standard stars.

Before applying the calibration to the science frames, the stars in the galaxy with a photometric error (`merr`, as calculated by IRAF) greater than 0.1 dex were removed, as were stars with errors reported in the centering algorithm (`sier`, `cier` or `pier` \neq 0). The remaining stars were then calibrated. First for aperture and exposure time, and then for extinction, time of

observation and zero-point through

$$m_i = m_{0,i} + k_i X + \alpha_i T + z_i,$$

where m is the star's magnitude, and constants and indices are as in Eq. (2.1).

In order to minimise the effect of noise and compensate for fluctuations in the observational conditions it is desirable to use as many frames as possible in the analysis. However, there may be an offset between the magnitudes of different exposures taken during the same night, even after having corrected for airmass and time (see Fig. 2.9).

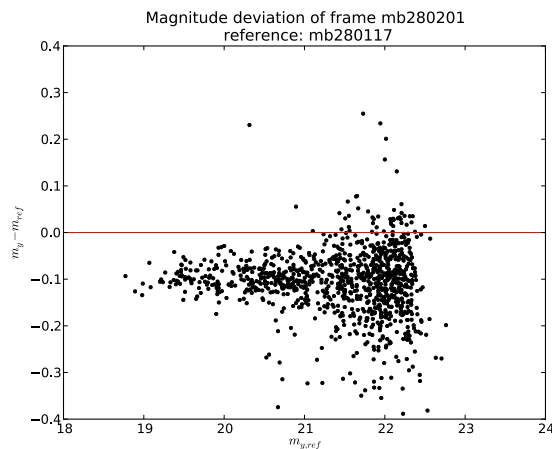


Figure 2.9 Deviation in magnitude from the stars in one frame to those of another.

Because there is no way of knowing which frame has a measurement closest to the "truth", all frames will be added together by means of averaging. However, their respective deviations from one another will be taken into account in the following way. The median flux value of every star is calculated across all frames within the respective filters. Every star in one particular frame then have a deviation from this value. The median of all these deviations is then taken to be the offset of the frame, and is added (or subtracted, depending on whether the offset is negative or positive) to its stars' flux values before averaging the frames. The median is preferable to the average here because the sensitivity to the effect of outliers decreases. This offset (m_{off}) is also added to the photometric errors of the frames:

$$\sigma_{phot} = \sqrt{\mathbf{merr}^2 + m_{off}^2}.$$

Note that since magnitude is a logarithmic unit, while the thing physically measured is flux, the average magnitude will not correspond to that of the

average flux. The magnitudes are therefore converted into units of flux before averaging. The final flux for each star is calculated by averaging the frames within each filter for each night, using the photometric errors as weights:

$$\bar{F} = \frac{\sum_{j=1}^n f_j / \sigma_{\text{phot},j}^2}{\sum_{j=1}^n 1 / \sigma_{\text{phot},j}^2}$$

where f is the flux of a star, σ_{phot} is the photometric error, j is the frame, and n is the total number of frames. By using the errors as weights in this manner, frames with a large offset from the others will affect the final fluxes less than frames which deviate less, further decreasing the sensitivity to outliers in the measurements.

Finally, the averaged fluxes are converted into magnitudes, and the colour correction is applied. Because the standard magnitudes for the stars in the science frames are not previously known, they are postulated as solutions for the following system of equations:

$$\begin{cases} m_y = m_{0,y} + a_y(m_v - m_y) \\ m_v = m_{0,v} + a_v(m_v - m_y) \\ m_b = m_{0,b} + a_b(m_v - m_y) \end{cases} \Rightarrow \begin{cases} m_y = \frac{m_{0,y} + \frac{a_y m_{0,v}}{1-a_v}}{1 + \frac{a_v a_y}{1-a_v} + a_y} \\ m_v = \frac{m_{0,v} - a_v m_y}{1-a_v} \\ m_b = m_{0,b} + a_b(m_v - m_y) \end{cases}$$

where m_0 here denotes observed magnitude corrected for airmass, time of observation and zero-point.

2.6 CMD and metallicities

The calibrated magnitudes were used for plotting a CMD for each night, see fig 2.10. In the diagram the RGB, HB, and some sub-giant stars are visible. The MSTO appears, however, to be too faint for detection in this study.

Metallicities were determined from the photometry through the m_1 index, using the semi-empirical relations of Calamida et al. (2007):

$$[\text{Fe}/\text{H}] = \frac{m_1 + a_1(v - y) + a_2}{a_3(v - y) + a_4}, \quad (2.2)$$

with coefficients $a_1 = -0.521 \pm 0.001$, $a_2 = 0.309$, $a_3 = 0.094 \pm 0.001$, and $a_4 = -0.099 \pm 0.005$. This calibration was chosen because it has shown

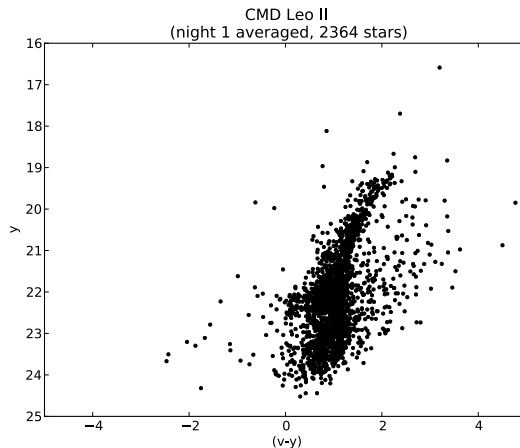


Figure 2.10 CMD of LeoII constructed from the observations of one night.

good agreement with spectroscopic metallicity determinations of RGB stars in globular clusters (Frank et al. 2015), and should thus be suitable for deriving the $[\text{Fe}/\text{H}]$ of giants in dSph galaxies from Strömgen photometry. The calibration is valid for $[\text{Fe}/\text{H}] = -2.2$ to -0.7 dex (since this was the metallicity range of the globular clusters used in the calibration), and so for lower or higher metallicities the determinations will not be as reliable.

2.7 Error estimation

The total photometric errors for each night are calculated through

$$\epsilon_{phot} = \sqrt{\frac{1}{\sum_{j=1}^n 1/\sigma_{phot,j}^2}},$$

where σ_{phot} is the combination of `merr` as yielded by IRAF and the offset of each individual exposure (as explained in § 2.5), and j is the exposure out of n total exposures in each filter.

For the total errors in the magnitudes the uncertainties in the calibration constants (k , a , α and z) must also be taken into account. However, these will only affect the zero-level of the photometry, and are not relevant for star-by-star comparisons within the data. These errors are in this work approximated by ϵ_z , as it was found in a similar study by Adén et al. (2009) that the uncertainty introduced by the calibration could be approximated by the uncertainty in zero-point only. Thus, the total errors are defined as

$$\epsilon_{tot} = \sqrt{\epsilon_{phot}^2 + \epsilon_z^2}.$$

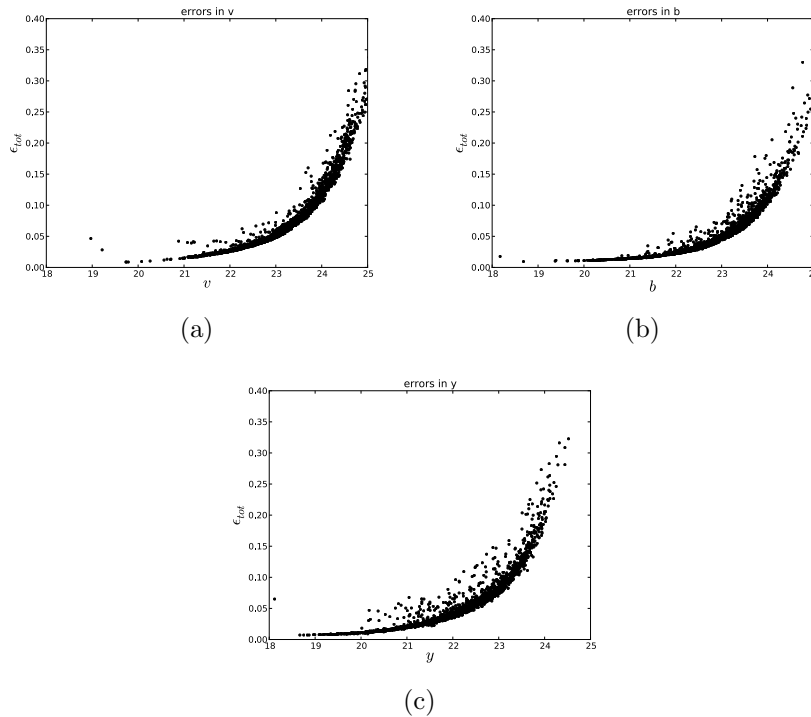


Figure 2.11 Total errors in the (a) v , (b) b and (c) y magnitudes.

The total errors in the respective magnitudes are plotted in Fig. 2.11.

The errors in metallicity were estimated through Monte Carlo simulations, following the procedure of Faria et al. (2007). This was done in the following way. For each magnitude of a given star (i.e. for each v , b and y), 5000 synthetic magnitudes were generated:

$$m_i = m_{0,i} + \Delta m,$$

where $m_{0,i}$ is the calibrated magnitude in filter i , and Δm is a random number drawn from a normal distribution with mean 0 and variance ϵ_{tot}^2 . From these magnitudes, 5000 sets of m_1 and $(v - y)$ were calculated.

The same thing was done for the coefficients of Eq. (2.2), where each coefficient was modified by adding a random number drawn from a normal distribution with mean 0 and variance equal to the square of its respective uncertainty, until 5000 sets of coefficients had been acquired (note however that a_2 lacks uncertainty and thus was kept constant throughout the simulations).

For each set of values, Eq. (2.2) was evaluated, and so 5000 synthetic metallicities were obtained for each star. From these a metallicity distribution function (MDF) was created for every star, see Fig. 2.12. The upper and

lower sextiles of the distribution (which would correspond to 1σ in a Gaussian distribution) were chosen to represent the errors. Note that the MDFs for the synthetic stars are not necessarily symmetric around the original value of $[\text{Fe}/\text{H}]$. The final errors were therefore defined as half the distance between the lower and upper sextile.

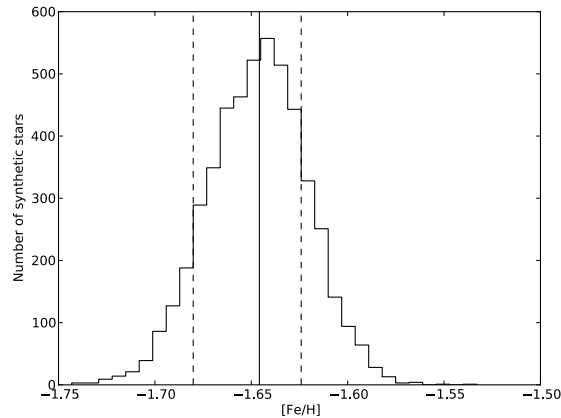


Figure 2.12 Distribution function of 5000 synthetic metallicities of one single star. The solid line marks the calibrated metallicity of the star in question, while the dashed lines mark the lower and upper sextiles of the distribution.

The final errors in $[\text{Fe}/\text{H}]$ are plotted in Fig. 2.13. It can be noted that the errors are generally larger for faint stars, and stars of low metallicity. Shown in Fig. (b) are stars with $\epsilon_{[\text{Fe}/\text{H}]} < 0.2$ dex, which amounts to 72 % of the total number of stars.

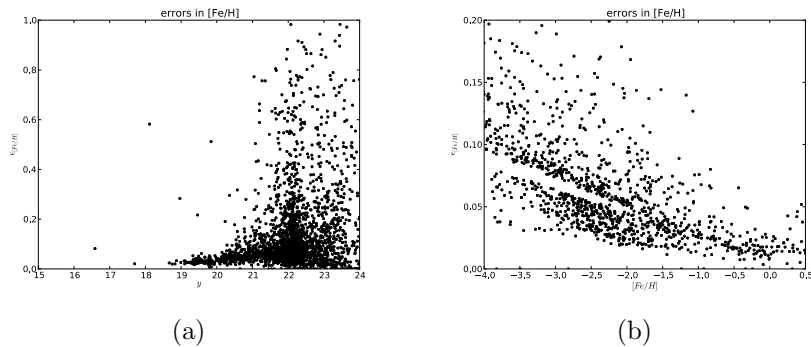


Figure 2.13 Errors in $[\text{Fe}/\text{H}]$ plotted against (a) y magnitude (b) $[\text{Fe}/\text{H}]$.

2.8 Comparing nights

In order to increase the statistical certainty of the observations it is desirable to add several images together. In § 2.5 is described how this is done for images taken during one and the same night. Before data from multiple nights of observations can be added together, though, it is necessary to ascertain that the quality of the observational conditions is good enough for the data to be usable. This is investigated by comparing the results from each respective night in the following way.

28 February (henceforth night 1) is according to the observational logs the night with best weather conditions. 1 and 2 March (henceforth nights 2 and 3, respectively) report clouds and worse seeing (though not quantified for any of the nights). Night 1 was therefore chosen as reference for the observations, and so nights 2 and 3 were compared individually with it and not with one another.

First all stars which had good measurements in both nights were identified (good here meaning having a magnitude calculated by IRAF with `merr` < 1 dex). In night 2 this amounted to 238 stars, and 274 stars in night 3. Only 15 stars had good measurements in all three nights. A first comparison was made by inspecting the CMDs of the overlapping stars in the respective nights, see Fig. 4.1. Already from these diagrams it is evident that the measurements differ significantly. It can be noted that in night 2 stars appear generally redder than in night 1. In night 3 bright stars appear fainter than in night 1, and faint stars appear brighter than in night 1, resulting in the shape of the RGB appearing compressed.

In order to quantify this deviation further the difference in measured magnitude (post calibration) of the stars in each filter during the respective nights were plotted, see Fig. 2.15. From the plots it is evident that most stars in night 2 deviate greatly from their magnitudes as measured during night 1, up to several magnitudes. There is a trend where the brightest stars appear fainter, and the faintest stars appear brighter. In night 3 the same trend, although to a lesser extent, can be noted.

Before deciding on whether or not nights 2 and 3 should be deemed useable a number of factors were considered as a cause of this deviation, in order to investigate whether anything could be done to compensate for it. Errors in the calibration might cause deviations in the photometry. However, erroneous airmass, time and zero-point calibration constants (k , α and z) would only affect the zero-point of the photometry, and not cause a magnitude-dependent offset like this. The colour-constant (a) is not a likely factor either, at least not by itself, considering it being very small (see Table A.2). A re-calibration of nights 2 and 3 was attempted using the

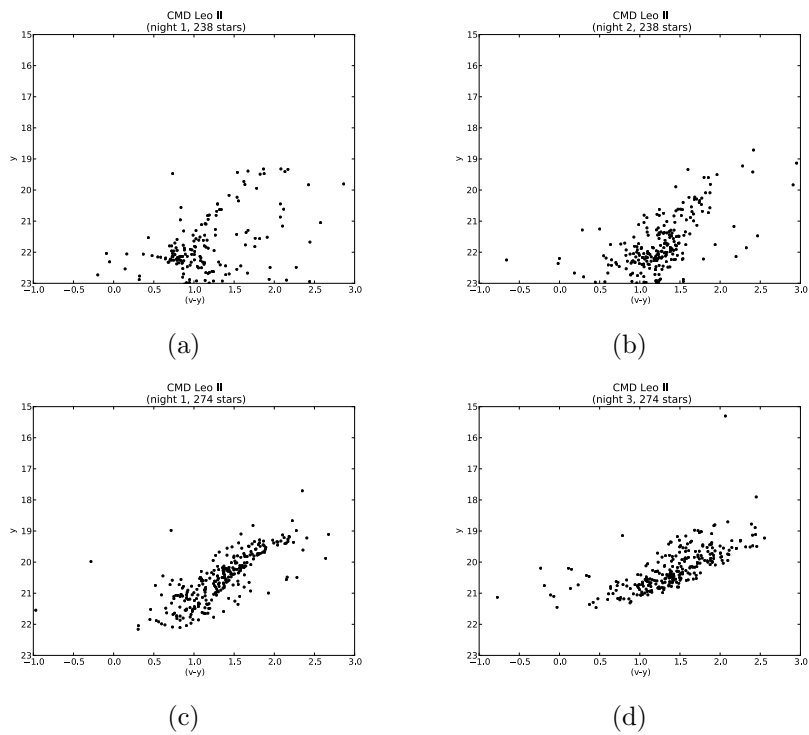


Figure 2.14 Comparisons of CMDs for nights 1, 2 and 3. (a) contains the stars with good measurements in nights 1 and 2, as measured during night 1. (b) contains the same stars, as measured during night 2. (c) contains the stars with good measurements in nights 1 and 3, as measured during night 1. (d) contains the same stars, as measured during night 3.

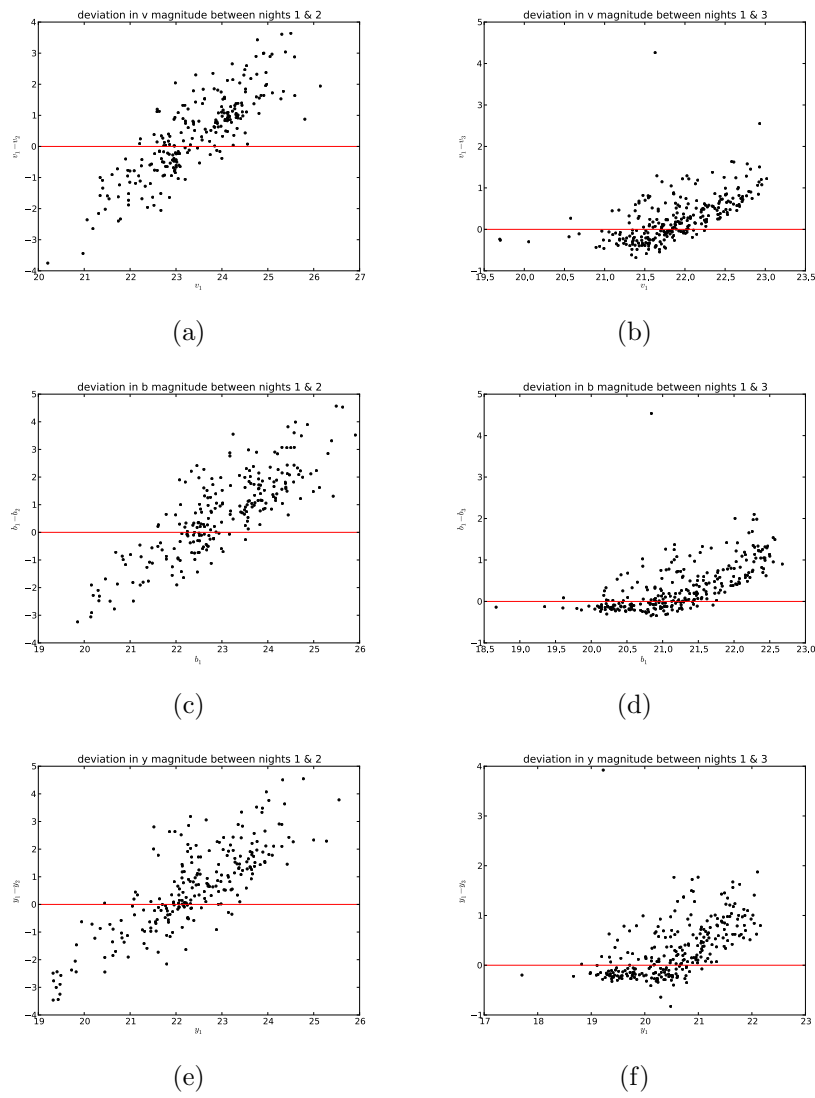


Figure 2.15 Differences in (calibrated) magnitudes between nights 1 and 2 in filters (a) v , (c) b and (e) y . Differences between nights 1 and 3 in filters (b) v , (d) b and (f) y .

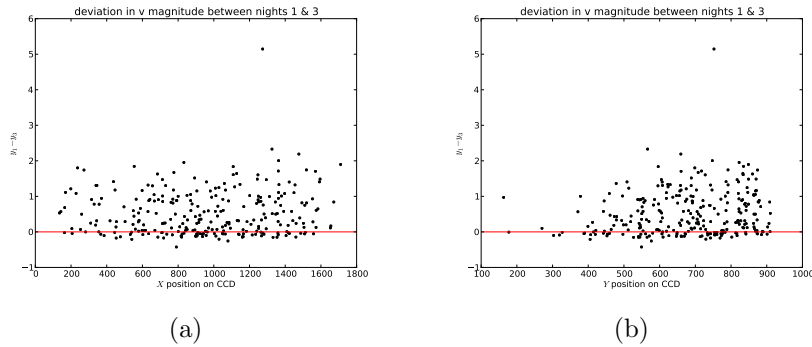


Figure 2.16 Deviation in y magnitude between nights 1 and 3, plotted against (a) X and (b) Y position on the CCD.

brightest stars of night 1 as standard stars. This did not affect the nature or magnitude of the deviations significantly.

Varying sensitivity at different parts of the CCD might cause stars to be measured systematically as brighter or dimmer depending on their location in the field of view. Flatfielding is intended to compensate for this, but in case any such effects remained the issue was investigated. Because the alignment of the fields of view on the CCD agree to within a few pixels between the exposures, this could be done simply by plotting the deviation in magnitude versus position on the CCD (see Fig. 2.16). Seeing as no trends are found with respect to position (apart from the lower fourth of the CCD generally yielding few good measurements), this was concluded to not be causing the deviation.

Left to consider were then the shapes of the stellar PSFs, and how they might affect the result of the aperture photometry performed upon them. Worse seeing means a larger FWHM of the PSFs, i.e. the stars appear more "smeared out" when weather causes the light to scatter to a larger degree in the atmosphere. An illustration of this is shown in Fig. 2.17. Just by looking at the stars in the frames themselves (left column) one can clearly see the effect of stars getting fainter and more smeared out with worse seeing.

The shapes of the PSFs (right column) confirm this. It is evident that stars which were resolved as separate during night 1 blend together or fade into noise during nights 2 and 3. This means that even if the size of the aperture is adjusted to equal the FWHM of the PSFs so that the stars are measured out to a sufficient extent, the wings of the PSFs of neighbouring stars might contaminate the measurements. Although the aperture correction takes care of correcting for the fact that the entire PSF is not encompassed by the aperture, there is no way of correcting for contaminating light

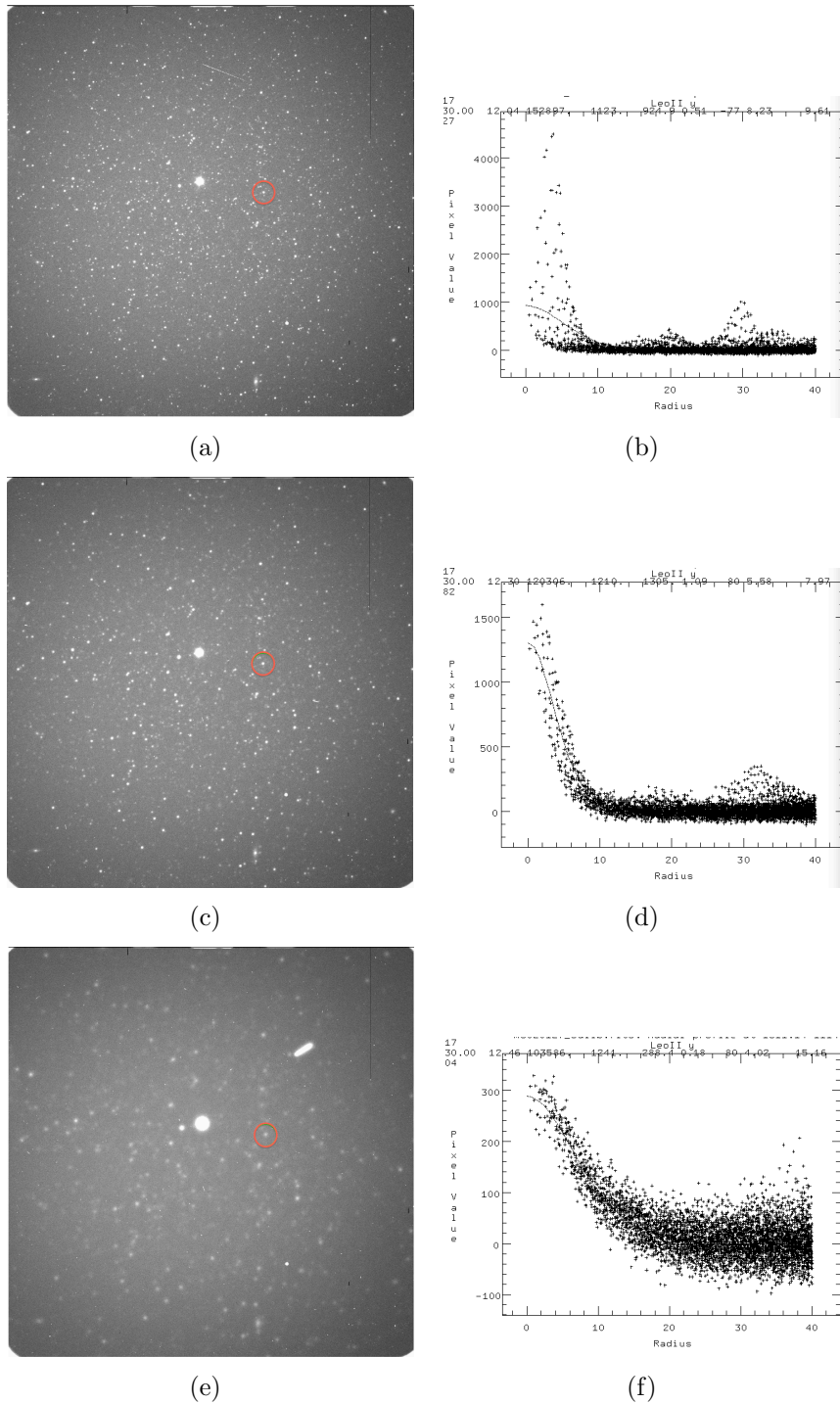


Figure 2.17 (a), (c) and (e) show three exposures of Leo II in the y filter made during nights 1, 2 and 3 respectively. The PSFs of the same close-lying group of stars (marked with a red circle) are shown in (b), (d) and (f) for nights 1, 2 and 3 respectively. Note how the PSFs lose in both intensity and distinction as the seeing grows worse.

from adjacent stars.

Leo II is a typically semi-crowded field (denser than stars in the average sky area but less crowded than a globular cluster) and thus fit for doing aperture photometry upon. However, from Fig. 2.17 it is clear that a field can turn from semi-crowded to crowded with bad seeing. This means not only that the stars blend into one another to a point of contamination (and sometimes melting together entirely), but also that the sky measurements might become polluted by stars to a troubling extent.

It can be concluded that bad weather is causing the deviation between the nights. The smearing out of the stellar PSFs would indeed result in faint stars appearing proportionally brighter, because light from neighbouring stars leaks into their apertures, while bright stars are proportionally less sensitive to contamination and thus simply appear less bright because more light is dispersed in the atmosphere. If the atmospheric conditions had been constant throughout the bad nights it might have been possible to compensate for this by means of a correction constant, but because cloud-cover can fluctuate a lot even during the time of one exposure (30 minutes) this is unfeasible without monitoring the weather variations in detail.

Some of the frames from nights 2 and 3 might be interesting for analysis through PSF photometry, where artificial PSFs are numerically fitted against the ones observed. In this kind of analysis it is possible to take blending in the wings of the functions into account. However, as this is beyond the scope of this work, nights 2 and 3 were deemed non-photometric for the purposes of aperture photometry, and were discarded from further analysis. Hence, all results from this study are based upon the data from night 1.

Chapter 3

Results

An excerpt from the table of results including coordinates, magnitudes, magnitude errors, metallicities, and metallicity errors is shown in Table. A.3. The full table of 2364 stars is available through contacting the author or Sofia Feltzing.

3.1 Colour-magnitude diagrams

A set of CMDs are shown in Fig. 3.1. The RGB is clearly visible, and also a HB at around $y = 22$. At magnitudes fainter than $y = 22$ are subgiants. It is evident that these observations do not go deep enough to discern the MSTO.

3.2 Metallicity

A MDF of Leo II is shown in Fig. 3.2. It is a so-called generalised MDF, constructed from the stars in the Monte Carlo simulation described in § 2.7. Each star is thus featured 5000 times, each time with a metallicity randomly drawn from a normal distribution centered on its metallicity, with a spread of the error in its metallicity. This is a way of weighting the calculation so that measurements with a large error will contribute less to the total, thus making the calculation less sensitive to both outliers and noise. The MDF peaks at $[\text{Fe}/\text{H}] = -2.4$, and has a spread (corresponding to half the distance between the lower and upper sextiles) of 1 dex.

A question of interest is whether or not the spatial distribution of stars of different metallicities is the same across the galaxy, or if e.g. there are concentrations of stars with certain metallicities. Such concentrations might indicate the presence of several stellar populations within the galaxy, which

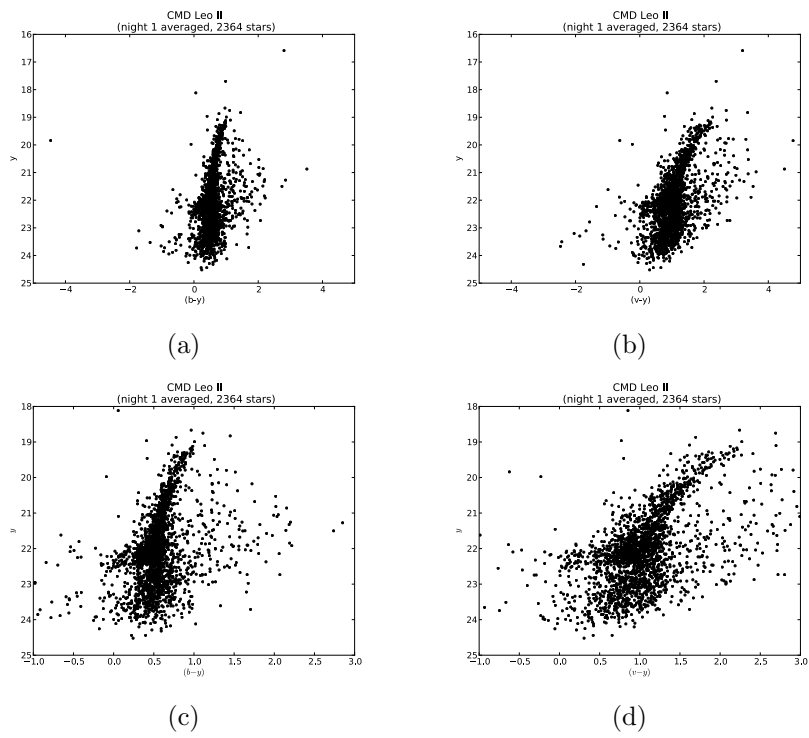


Figure 3.1 CMD for Leo II in colours (a) $(b - y)$, and (b) $(v - y)$, including 2364 stars with $\epsilon_{tot} < 0.4$. (c) and (d) zoom in on the interesting features.

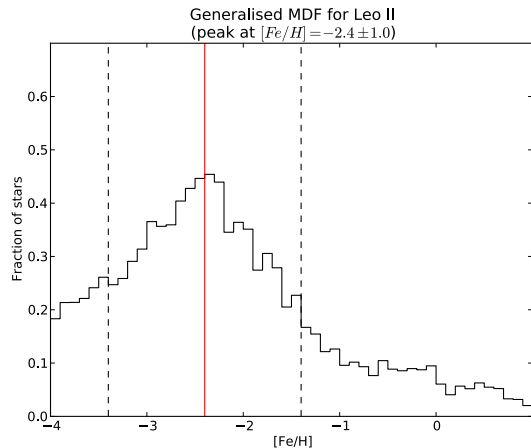


Figure 3.2 Generalised metallicity distribution function for Leo II, constructed from Monte Carlo simulated synthetic stars. Peak and spread corresponding to upper and lower sextiles of distribution are marked with red and dashed lines, respectively.

in turn could give clues concerning its SFH. The spatial metallicity distribution is illustrated in Fig. 3.3, where the stars are plotted with respect to metallicity and position in the galaxy. From visual inspection it appears that the distribution is not entirely uniform.

In order to investigate this statistically the galaxy was divided into quadrants, the MDF of which are shown in Fig. 3.4. The stars were in turn divided into seven bins of different metallicity ranges, starting from -3.5 dex and ending at 0 dex, in steps of 0.75 dex. All stars of $[\text{Fe}/\text{H}] > 0$ and $[\text{Fe}/\text{H}] < -3.5$ were grouped into two bins, respectively.

A χ^2 test was then performed with the null hypothesis that the metallicity distribution (i.e. the number of stars belonging to each of the metallicity bins) of all the respective quadrants is similar enough to belong to the same population. A confidence level of 1% was set, meaning that if the P value obtained from the χ^2 value via the cumulative distribution function is < 0.01 , the null hypothesis should be rejected. The test yielded $P \approx 4.7 \times 10^{-5}$, and the conclusion is thus that the distributions are not the same, i.e. that the spatial distribution of stars of different metallicities varies across the galaxy.

Further investigation of whether the MDFs of the quadrants differ significantly from one another was made using a Kolmogorov-Smirnov (KS) test which considers the maximum deviation between the normalised cumulative distributions. Also this test yielded the result that the MDFs differ signific-

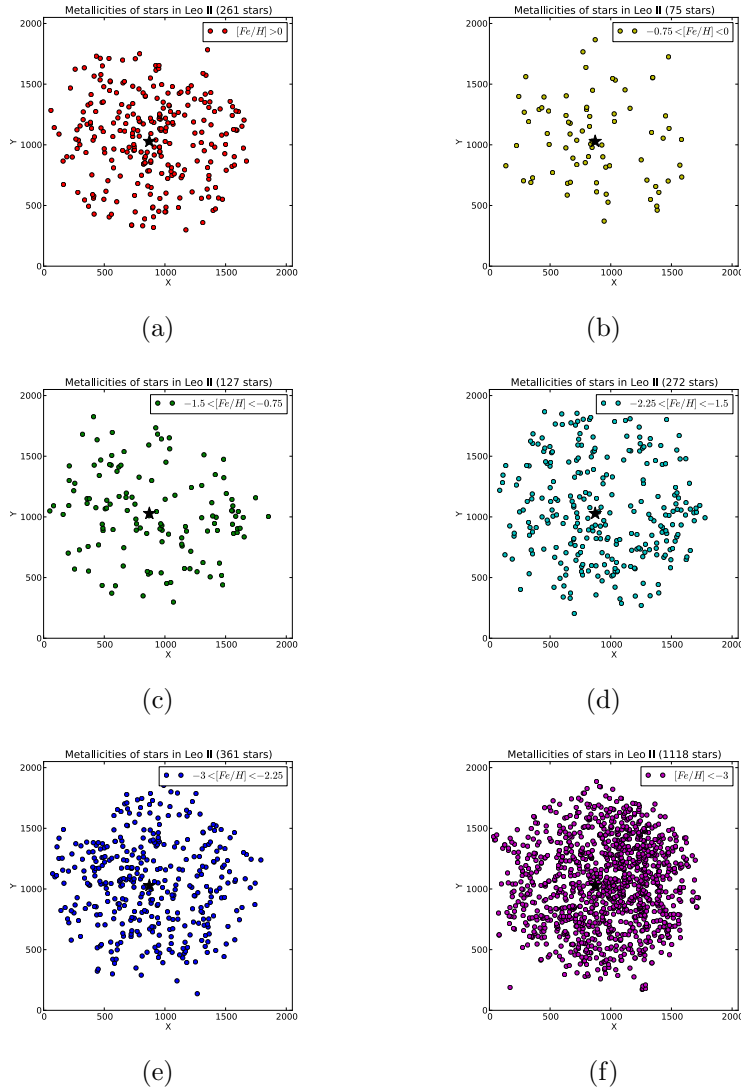


Figure 3.3 The spatial distribution of stars of different metallicities in the galaxy, plotted against coordinates on the CCD. The metallicity is binned according to (a) $[Fe/H] > 0$, (b) $-0.75 < [Fe/H] < 0$, (c) $-1.5 < [Fe/H] < -0.75$, (d) $-2.25 < [Fe/H] < -1.5$, (e) $-3 < [Fe/H] < -2.25$, and (f) $[Fe/H] < -3$. The black star indicates the centre of the Leo II galaxy.

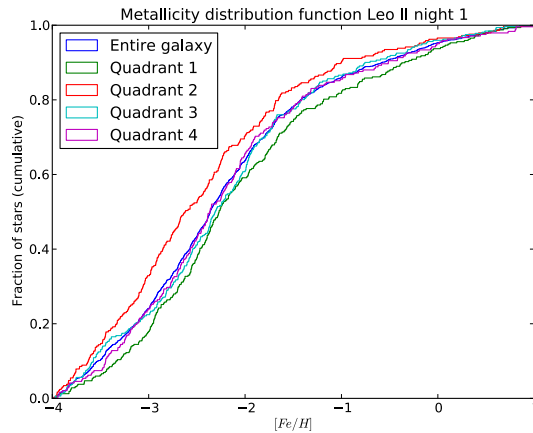


Figure 3.4 Cumulative metallicity distribution functions for the quadrants in Leo II, normalised for ease of comparison. Quadrant 1 corresponds to the upper right corner, 2 lower right, 3 lower left and 4 upper left.

antly from one another. The same result is obtained when dividing the field into 16 parts and comparing them with one another.

The SFH of a galaxy tends to vary with distance to the galactic centre. Therefore, the metallicities of the stars were plotted with respect to their radial distances to the centre (see Fig. 3.5). A metallicity gradient of -0.220 ± 0.016 dex/ r_c was found through a least-squares linear fit, with uncertainties in metallicities taken into account. In this investigation only stars with metallicities ranging between -4 and 0.5 dex, with $\epsilon_{phot} < 0.1$ dex, and $\epsilon_{[Fe/H]} < 1$ dex were used. The stars closest to the galaxy's centre are missing because of their large uncertainties. Note that at no radius does the fitted line go through the median metallicity (-2.4 dex) of the dSph galaxy. This is because the fit is weighted by the metallicity errors, so that stars with low uncertainties (generally stars of higher metallicities, see Fig. 2.13(b)) affect the fit more strongly than stars with high uncertainties.

Furthermore, the MDFs of concentric circular segments of the galaxy were investigated (see Fig. 3.6). A tendency can be discerned where the innermost part of the galaxy is fractionally more devoid of metal-poor stars, while its outermost regions shows a deficit of metal-rich stars. It thus appears that metal-rich stars cluster towards the centre.

Another interesting thing to consider regarding the stars' metallicities is their evolutionary stage. This was done by colour-coding the metallicities into the CMD, as shown in Fig. 3.7. In general terms the tip of the RGB is dominated by metal-poor stars, while the stars of highest metallicity cluster

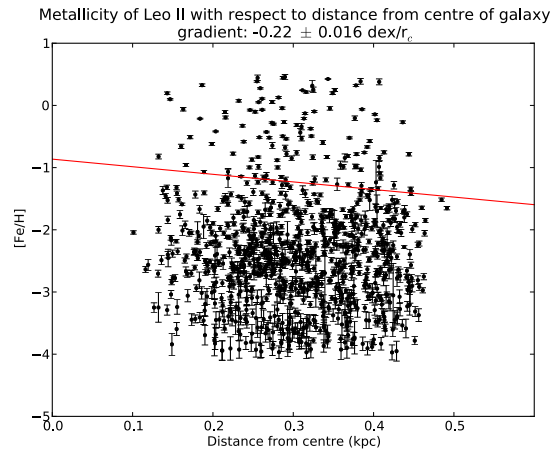


Figure 3.5 Metallicities of stars in Leo II with respect to their radial distance to the galaxy’s centre. A least-squares linear fit is represented by the red line. The error bars represent the metallicity uncertainties.

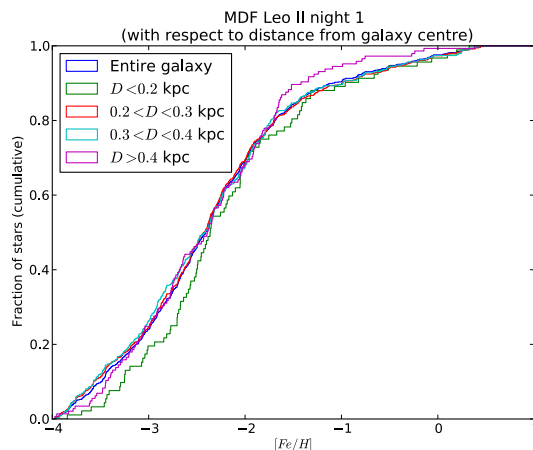


Figure 3.6 Normalised, cumulative metallicity distribution functions of concentric annuli in Leo II. D denotes distance from the galaxy’s centre.

closer to the MSTO. There is also a tendency in the RGB of more metal-rich stars appearing redder, which is to be expected (as explained in § 1.3).

Further insight into the stars’ properties can be gained through the m_1 index. Since this is a measure of the total intensity of the metal absorption lines, stars will occupy different regions of an m_1 plot depending on their metallicities, see Fig. 3.8. In Fig. 3.8(a) HB (blue markers) and RGB (red markers) stars can be seen to congregate to the left and right of the plot,

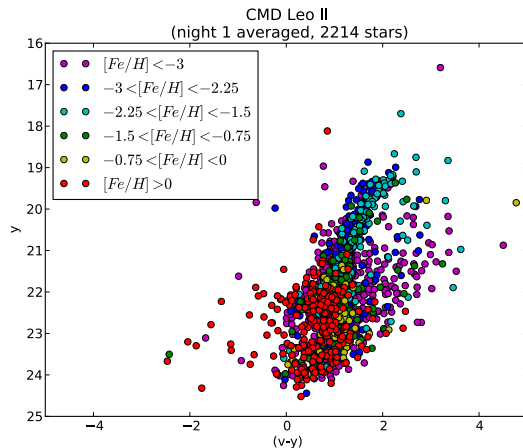


Figure 3.7 CMD of Leo II with metallicities colour-coded. Only stars with $\epsilon_{[\text{Fe}/\text{H}]} < 1$ are shown.

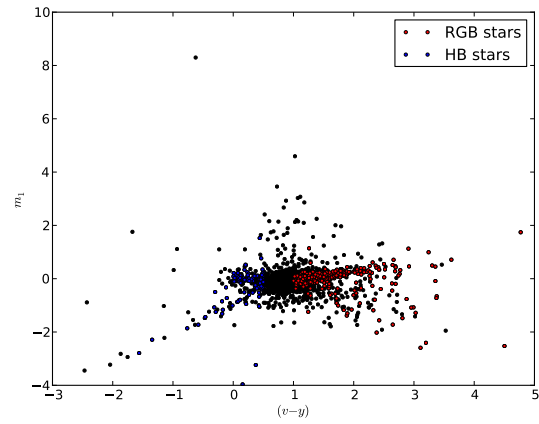
respectively. Remaining stars (black markers) are likely sub-giants or dwarf stars. Outliers are likely to be foreground Galactic stars. These stars (191 in total) were therefore removed from the CMD in order to clean it up. The final CMD is shown in Fig. 4.1(d).

Because the metallicity calibration (of Calamida et al. (2007), see Eq. (2.2)) is valid only for giant stars, it is interesting to take a closer look at part of the m_1 diagram. Only the RGB stars are shown in Fig. 3.8(b). Here are also plotted isometallicity lines based on the calibration. While there is a certain spread, it is evident that the bulk of the stars in Leo II have a metallicity lower than -2 dex.

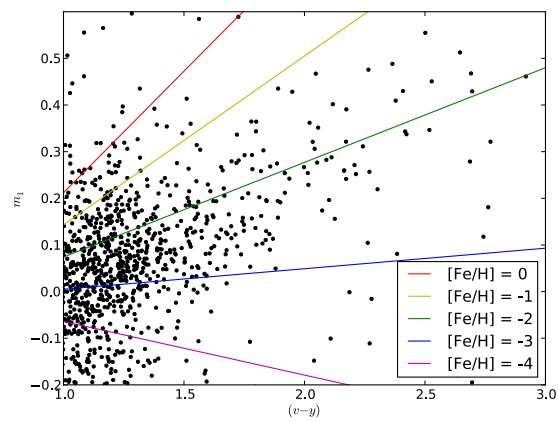
3.3 Membership determination

When looking at a faraway galaxy such as Leo II, the line of sight will inevitably go through the disk of the Milky Way. Therefore, the field of view will be contaminated by foreground stars. Because a close-by faint star and a faraway bright star will look similar in terms of magnitude, and possibly even end up in the same place in the CMD, it is not possible to distinguish between stars belonging to the dSph galaxy and foreground stars belonging to the Milky Way by means of magnitude alone.

The only certain way of determining whether or not a star belongs to a dSph is by measuring its radial velocity to see if it falls within the galaxy's velocity distribution. This is done by measuring the doppler shift of absorption lines in the stellar spectra, and so requires spectroscopic measurements.



(a)



(b)

Figure 3.8 m_1 plotted against $(v - y)$ for (a) all observed stars. HB stars are marked in blue, and RGB stars in red. (b) RGB stars only. Isometallicity lines from the calibration of Calamida et al. (2007) are overlotted.

Such studies have been made of Leo II by e.g. Kirby et al. (2011) and Spencer et al. (2017). We find in total 152 stars which (based on their sky coordinates) overlap with spectroscopic studies, and shall thus use these stars for comparisons in our discussion (see § 4.2).

In the meantime, we can make estimations regarding the expected amount of foreground stars. This was done by means of using the TRILEGAL online tool for simulating the stellar density and photometry for a given sky area (for details on the project and simulation, see e.g. Vanhollebeke et al. 2009). The distribution for our field of view is overplotted against our CMD in Fig. 3.9. From this can be inferred that while a few of the simulated stars line up along the RGB, most of the Galactic stars are expected to fall outside it. So while no definitive conclusions can be drawn about any specific stars in this manner, we get an indication that outliers are more likely to belong to a Galactic foreground population than to Leo II, and also that foreground stars are relatively few.

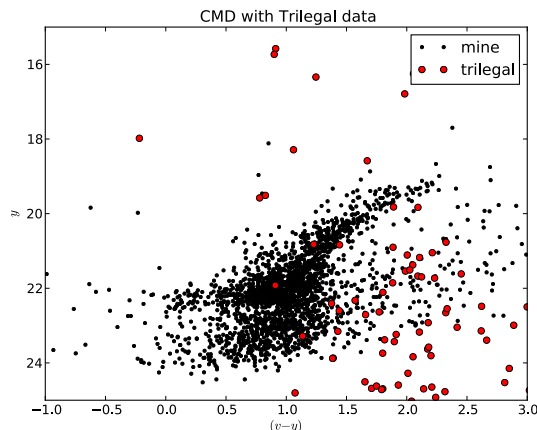


Figure 3.9 Galactic stars in our field of view as simulated by TRILEGAL, overplotted against our CMD.

3.4 Age determination

In order to determine the age of the stars in Leo II, isochrones with a $[\text{Fe}/\text{H}] = -2.4$ were obtained from the PADOVA online database (Marigo et al. 2017). When shifted by a distance modulus of 22.1 dex (determined by means of visual inspection), corresponding to a distance of 363 kpc, these line up nicely with the RGB of the galaxy (see Fig. 3.10). As very few stars are located

bluewards of the 6 Gyr isochrone, it would appear that the bulk of the stars in Leo II are older than this.

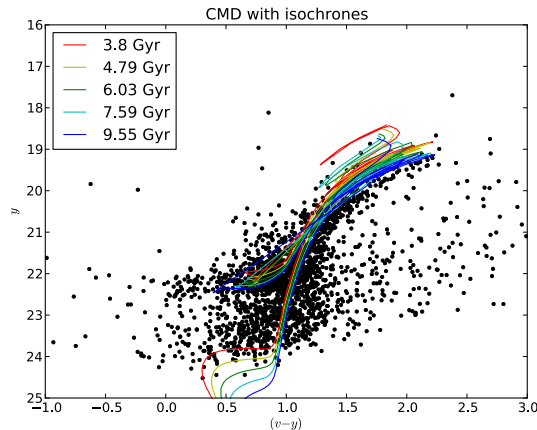


Figure 3.10 Isochrones of $[\text{Fe}/\text{H}] = -2.4$ dex, shifted with a distance modulus of 22.1 dex.

However, as is evident in the plot, the isochrones of ages greater than 6 Gyr lie close enough to one another to be indistinguishable compared to the spread of our data. This is common in the study of giant stars, because the RGB looks much the same for isochrones of the same metallicity. As can also be seen in the plot, the isochrones have a larger spread around the MSTO. Therefore, had our data extended down to faint enough magnitudes to include this region, age determination in this manner might have yielded more nuanced results. It does, however, serve well to remember that a dSph galaxy, in contrast to most globular clusters, contain several stellar populations, and that isochrone fitting does not necessarily distinguish between them. Furthermore, this means that the dSph galaxy contains a spread in metallicity, which further complicates the interpretation of the isochrone fitting.

3.5 Morphology

In an attempt to map the structure of Leo II, its stellar density was plotted with respect to position in the galaxy, see Fig. 3.11. As would be expected for a dSph galaxy, the density appears to be highest at its centre and decrease towards its outskirts. There appears, however, to exist a morphology more complex than concentric sphericalness.

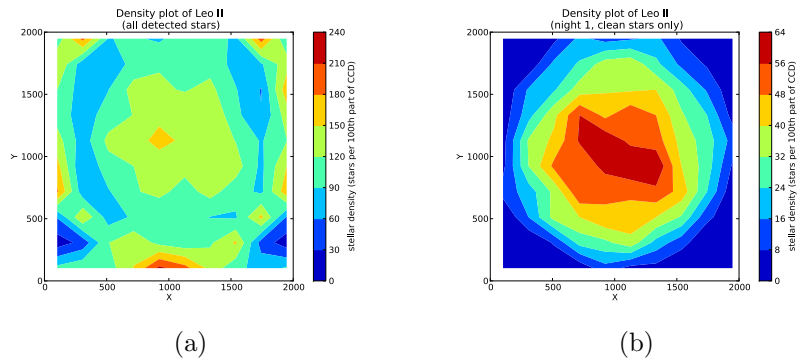


Figure 3.11 (a) Stellar density of Leo II (including all detected objects which could possibly be stars). (b) Stellar density of Leo II (only stars with $\epsilon_{phot} < 1$ included).

Chapter 4

Discussion

Having all the answers just means you've been asking boring questions.

— Joey Comeau

4.1 Literature comparisons: photometry

Although this is the first photometric study of Leo II using the Strömgen system, several other photometric studies have previously targeted the dSph galaxy. In Fig. 4.1 is shown the CMDs of three of these: Bellazzini et al. (2005), Koch et al. (2007), and Komiyama et al. (2007), in comparison with our own. Even though the photometric systems are not the same, and the colours thus not interchangeable, it is evident that the general shape of the CMD is similar across the studies. The tip of the RGB is located around $V = y = 19$, while the HB sits at around $V = 22$. Only Komiyama et al. (2007) goes deep enough to include the MSTO, which is to be found at around $V = 25$. Since our photometry only reaches down to around $V = 24$, it is evident that the MSTO is indeed unavailable for us to use for age determination (see § 3.4).

4.2 Literature comparisons: spectroscopy

As mentioned above, Leo II has been the target of several spectroscopic studies. We cross-correlated our data (based on the stars' sky coordinates) with four of the more recent ones: Siegel & Majewski (2000), Koch et al. (2007), Kirby et al. (2011) and Spencer et al. (2017), finding in total 152 stars which are decidedly members of Leo II based on their radial velocities. These are marked in a CMD in Fig. 4.2. Three of the studies targets RGB stars, while Siegel & Majewski (2000) targets mainly HB stars.

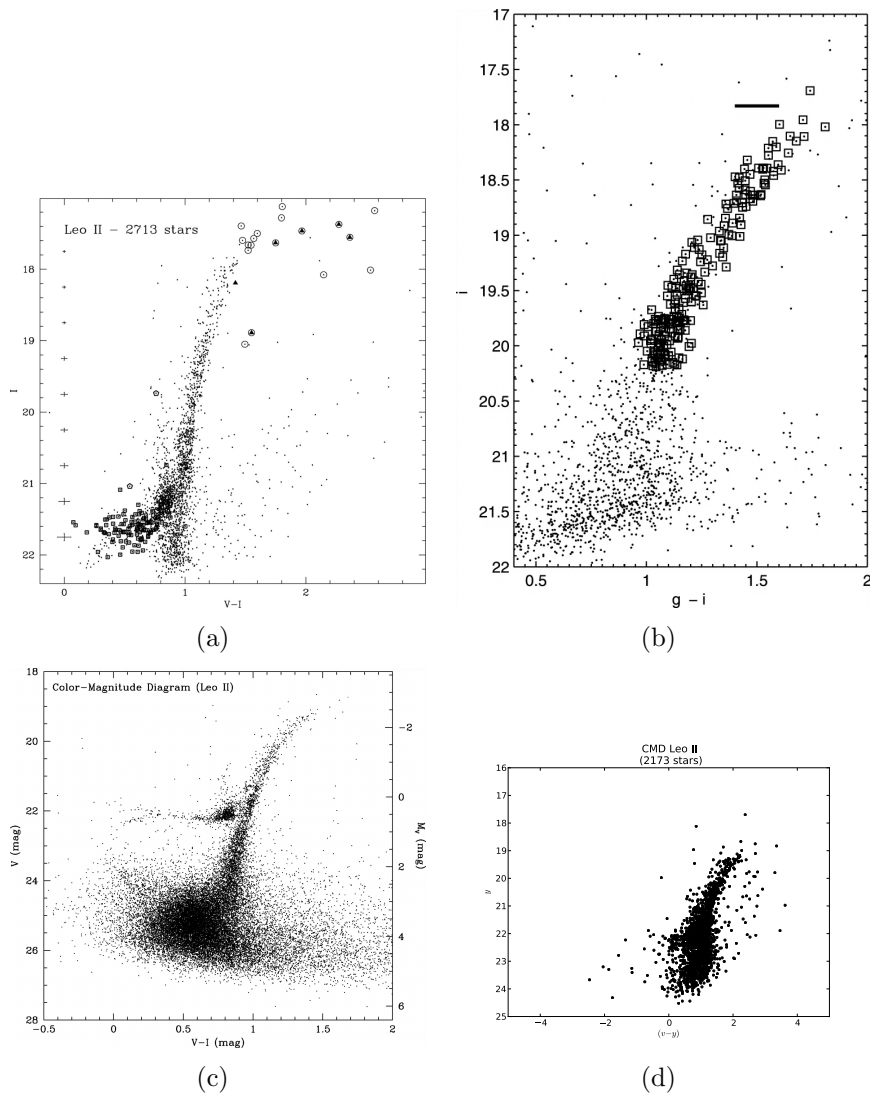


Figure 4.1 CMD of Leo II from (a) Bellazzini et al. (2005), (b) Koch et al. (2007), (c) Komiyama et al. (2007), (d) this study.

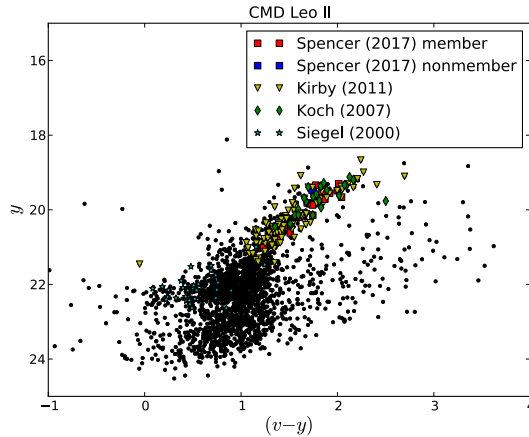


Figure 4.2 CMD marking Leo II members as identified in spectroscopic studies by Koch et al. (2007), Siegel & Majewski (2000), Kirby et al. (2011) and Spencer et al. (2017).

The total number of stars measured in these four studies greatly exceeds 152. The reason for not all of these showing up in our study is partly that the spectroscopic studies targeted stars from a considerably larger sky area than our field of view. For the stars within our field of view, some have bad photometry, i.e. yielding no magnitudes in the analysis and thus impossible to compare with. Better statistics, i.e. more photometrically good nights of observation, would likely have increased the number of stars for comparison. Only one star among ours has been identified as belonging to a foreground population (by Spencer et al. 2017).

In Siegel & Majewski (2000) 148 RR Lyrae type variable stars were identified as members of Leo II. Spectra were obtained for 140 of these, measuring their magnitudes, amplitudes and periods. Their average period was found to be 0.62 days, with amplitudes up to 2 mag. Hence, the magnitudes of these stars would be expected to change noticeably during the course of our observations. We found 32 stars overlapping with ours. The deviation in y (or V) magnitudes is shown in Fig. 4.3, with the amplitudes of the stars' variation indicated as error bars. Our measurements fall within the amplitudes for all but two stars.

In Koch et al. (2007), 197 stars in total were observed via medium-resolution spectroscopy. 52 of these were determined via radial velocity determination to be RGB stars belonging to Leo II, spread across the entire surface area of the galaxy. The study found a MDF peaking at $[\text{Fe}/\text{H}] = -1.74$ dex, with an asymmetrical shape extending towards low metallicities (see

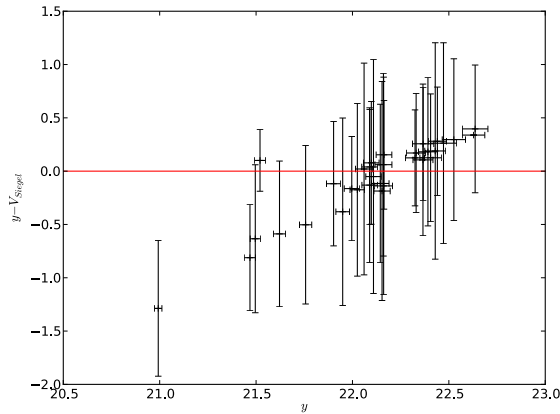


Figure 4.3 Deviation in y (V) between RR Lyrae variable stars in common for this study and that of Siegel & Majewski (2000). Error bars indicate the amplitude of the magnitude variation.

Fig. 4.4(a)). They find a full range of metallicities between -2.4 and -1.08 dex, and no radial metallicity gradient.

We found 23 stars overlapping with those of Koch et al. (2007). The deviation in y (corresponding to V), and also the deviation in metallicity, between stars in common between the respective studies is shown in Fig. 4.5. The magnitudes (except for one star) agree to within 0.1 dex, but still fall outside the errors of the respective measurements, the stars of Koch et al. (2007) appearing systematically brighter. The metallicities, in turn, deviate up to 1.5 dex from one another, increasing with decreasing metallicity.

In Kirby et al. (2011), the spectra of 294 RGB stars were measured, 258 out of which were determined to be members based on their radial velocities. The mean metallicity was found to be -1.62 ± 0.01 dex, and also this study finds an asymmetric MDF extending towards lower metallicities (see Fig. 4.4(b)). In contrast to Koch et al. (2007), they find a metallicity gradient of -0.21 ± 0.01 dex/ r_c . Note that in this study the distance to Leo II is assumed to be 219 kpc, which would contribute to a steeper gradient than a larger distance such as ours of 233 kpc would.

We found 99 stars overlapping with those of Kirby et al. (2011), 11 of which are in common with those of Koch et al. (2007). The deviation in y (corresponding to V), and also the deviation in metallicity, between stars in common between the respective studies is shown in Fig. 4.6. The magnitudes (except for one star) agree to within 0.2 dex, but for the most part fall outside the errors of the respective measurements, the stars of Kirby et al. (2011)

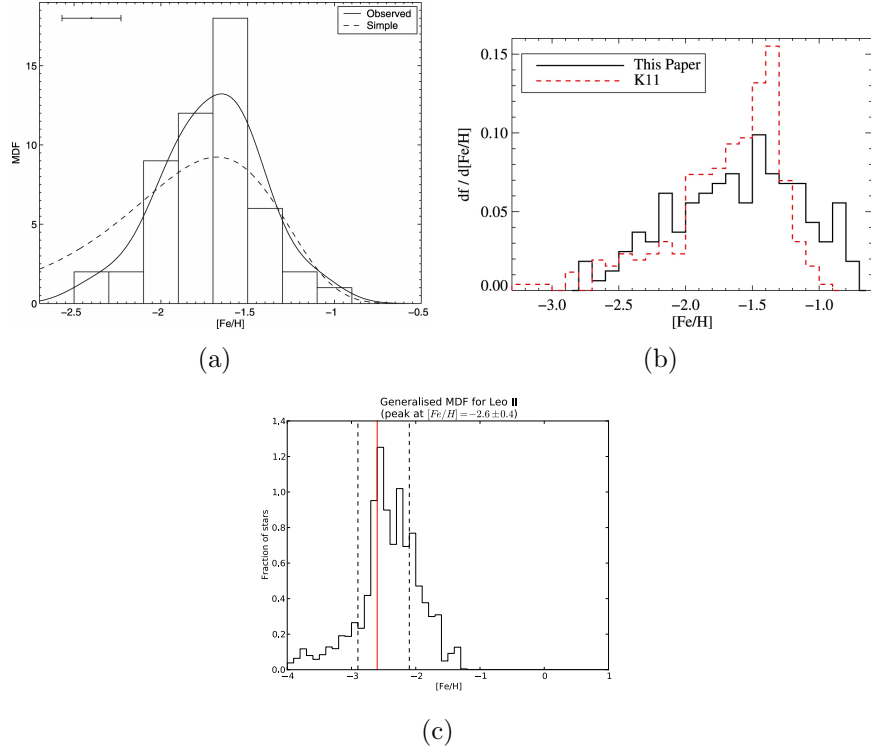


Figure 4.4 Metallicity distributions of (a) Koch et al. (2007), (b) Kirby et al. (2011) (dashed line) and Spencer et al. (2017) (solid line), (c) this study (including only confirmed Leo II members).

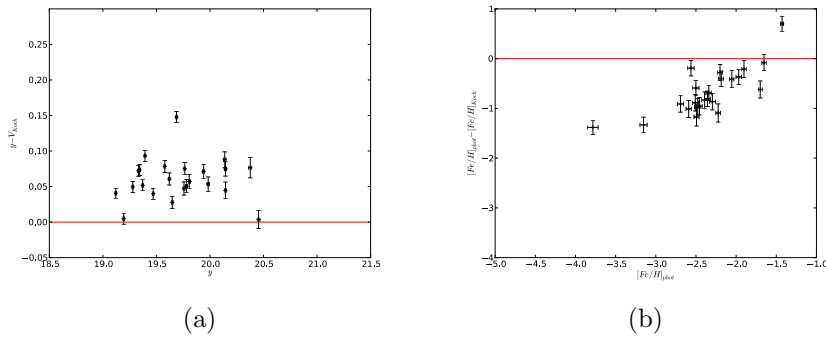


Figure 4.5 Deviation in (a) y (V) and (b) [Fe/H] between stars in common for this study and that of Koch et al. (2007). Vertical error bars indicate a combination of errors: $\epsilon = \sqrt{\epsilon_{\text{phot}}^2 + \epsilon_{\text{Koch}}^2}$.

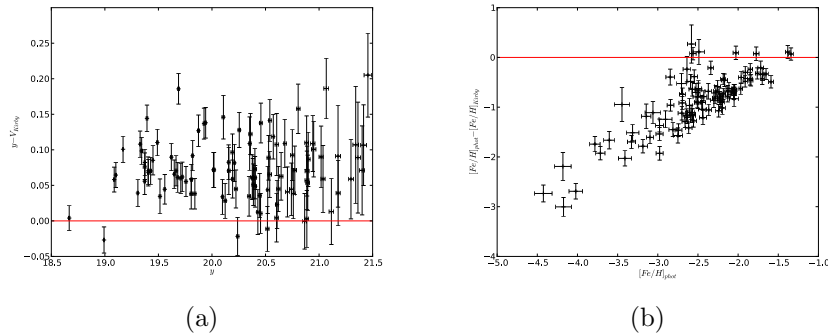


Figure 4.6 Deviation in (a) y (V) and (b) $[Fe/H]$ between stars in common for this study and that of Kirby et al. (2011). Error bars indicate a combination of errors: $\epsilon = \sqrt{\epsilon_{\text{phot}}^2 + \epsilon_{\text{Kirby}}^2}$.

appearing systematically brighter. The metallicities, deviate up to 3 dex from one another, increasing with decreasing metallicity.

In Spencer et al. (2017) 336 stars were observed spectroscopically, 258 of which were determined to be members of Leo II based on their radial velocity. The mean metallicity was determined to -1.70 ± 0.02 dex, also here with an asymmetric MDF extending towards low metallicities (see Fig. 4.4(b)). A radial metallicity gradient of -0.275 ± 0.1 dex/ r_c was found, assuming a distance of 233 kpc.

We found 19 stars overlapping with those of Spencer et al. (2017), 1 of which is in common with those of Koch et al. (2007), and 7 in common with Kirby et al. (2011). Out of these we identified one of our stars as a foreground star as it had been identified by Spencer et al. (2017) as not belonging to Leo II. The deviation in metallicity between stars in common between the respective studies is shown in Fig. 4.7. Because the study offers no magnitudes readily comparable to the Strömgren system, no magnitude comparisons can be made. The metallicities deviate up to -3 dex, increasing with decreasing metallicity.

Fig. 4.4(c) shows the MDF of all confirmed Leo II members of this study. We find a lower peak metallicity ($[Fe/H] = -2.6$ dex) than those of the studies compared with, but a similar overall behaviour with no stars of $[Fe/H] > -1$, and a tail extending towards lower metallicities. In summary, our measurements yield lower metallicities than all the spectroscopic studies we have compared with. This might indicate that our metallicity calibration is not reliable for Leo II. However, it should also be noted that spectroscopic and photometric metallicities are not entirely interchangeable. Furthermore,

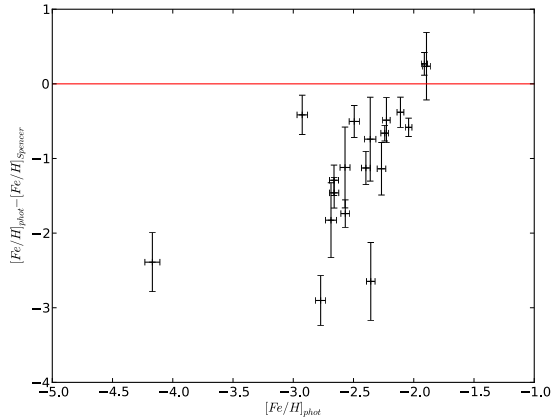


Figure 4.7 Deviation in $[\text{Fe}/\text{H}]$ between stars in common for this study and that of Spencer et al. (2017). Error bars indicate a combination of errors: $\epsilon = \sqrt{\epsilon_{\text{phot}}^2 + \epsilon_{\text{Spencer}}^2}$.

the photometric metallicity calibration is very magnitude-sensitive, so that a small change in magnitude between the filters gives rise to a large, non-linear change in metallicity. Seeing as there appears to be a systematic magnitude offset where our magnitudes appear fainter than in the studies compared with here, it is reasonable to expect the metallicity determinations to disagree. This offset is not necessarily caused by a faulty photometric procedure. It is common for offsets of up to a few tenths of a magnitude to occur between photometric results, due to factors such as the detector, or the calibrations of the photometric systems themselves.

Chapter 5

Summary

In February–March 2003, stars in the direction of the dSph galaxy Leo II were observed using Strömgren photometry, during three consecutive nights. In this project aperture photometry has been performed upon the data. From the data reduction it was concluded the two latter of these three nights were non-photometric, and thus all results of the study are based upon the observations (three frames in each of the filters v , b and y) of the first night only.

Magnitudes were obtained for 2364 stars in total, producing a CMD where the RGB, HB, and some subgiant stars are visible. The observations are however not deep enough to include the MSTO, and so age determination via isochrone fitting had to be done through fitting the tip of the RGB. The fit resulted in a distance modulus of 22.1 in the y filter, corresponding to a distance of 263 kpc (which is 30 kpc further than the conventionally used distance of 233, as measured by Bellazzini et al. 2005). The fit indicates that the youngest population of Leo II is at least 6 Gyr, but fails to discern any details regarding multiple populations.

Metallicities were determined using the calibration of Calamida et al. (2007). While metallicities are published for all stars, it should be noted that the calibration is only valid for giant stars. We find an asymmetric metallicity distribution which peaks at $[\text{Fe}/\text{H}] = -2.4$ dex, has a spread of 1 dex, and extends towards low metallicities.

We also find signs of a non-uniform spatial metallicity distribution where metal-rich stars clustering towards the centre, and a radial metallicity gradient of -0.22 ± 0.016 dex/ r_c . In terms of SFH, this implies that star formation was first quenched in the galaxy’s outskirts, and then continued in one or several later bursts in the galaxy’s central region. We also find signs of a morphology and metallicity distribution more complex than concentric sphericalness, although this is not investigated in detail.

Our observations were cross-correlated with four spectroscopic studies, revealing in total 152 stars which are members of Leo II based on their radial velocity. Based only on these, the metallicity peaks at $[\text{Fe}/\text{H}] = -2.6$ dex and has a spread of 0.4 dex. Magnitudes are generally fainter than those from the studies compared with, and the metallicities lower.

Had there been more time allotted to this project there is more work that could have been done with this data. Apart from applying for more observational time, for a follow-up study we would recommend the following.

Doing PSF photometry for all three nights of observation. For the purposes of aperture photometry only night 1 is deemed useable, but if nights 2 and 3, or even parts of them, would prove fit for analysis through PSF photometry, that would increase the statistics, and make for more solid magnitude measurements.

Another very useful thing would be to derive a new metallicity calibration for the Strömgren photometric system, seeing as the one of Calamida et al. (2007) seems to yield suspiciously low metallicities and also breaks down for stars of $[\text{Fe}/\text{H}] < -2.2$. This would be done using the spectroscopic metallicities for the stars overlapping with the studies of e.g. Koch et al. (2007), Kirby et al. (2011) and Spencer et al. (2017), in a multilinear regression together with the photometric colours against the m_1 index. In this way, new coefficients would be obtained for Eq. (2.2), which would hopefully yield a more solid determination of $[\text{Fe}/\text{H}]$.

With more solid metallicity determinations, isochrone fitting could be performed in greater detail, taking the spread of metallicities into account. A way to go about this would be to plot stars within a given (narrow) metallicity range only, and fit isochrones of the corresponding metallicity, thus determining the ages of the stars in different metallicity ranges separately.

Seeing as we have multiple exposures of confirmed RR Lyrae variable stars, one could use the magnitudes yielded from each exposure to construct time sequences. This might also reveal more variable stars within the galaxy.

In conclusion, there is a lot to be learned about the stars in a dSph galaxy by means of Strömgren photometry. We would recommend this procedure for follow-up studies of Leo II, and also for studies of other dSph galaxies, in the hope of furthering the detailed understanding of these distant, starry worlds.

Acknowledgements

This has been a work long in the making. There have been many obstacles, of both personal and scientific nature. I would like to thank the people without whose help this thesis would not have come to its conclusion.

First of all, thanks are due to Sofia Feltzing for being a patient and helpful supervisor.

Thank you to Luca Casagrande for teaching me the ways of photometry.

Thank you to Daniel Carrera for helping me out with statistics and programming.

Thank you to Pieter Gruyters for helping me out with photometry, proofreading my thesis, advising me on how to finish my results, and just generally being an awesome help on very short notice.

Thank you to Daniel Michalik for teaching me how to use a telescope, and with your stargazing nights reminding me of why I love astronomy when I needed it the most.

Thank you to Anna Árnadóttir for neverending encouragement, and for being the best boss that anyone could ever ask for.

Thank you to Eva Jurlander for always being so helpful and kind.

Last but not least, thank you to friends and family for believing in me all this time. You're the best support anyone could ever ask for, and I am glad beyond what words can express to have you all in my life.

Bibliography

- Adén, D., Feltzing, S., Koch, A., et al. 2009, *A&A*, 506, 1147
- Árnadóttir, A. S., Feltzing, S., & Lundström, I. 2010, *A&A*, 521, A40
- Bellazzini, M., Gennari, N., & Ferraro, F. R. 2005, *MNRAS*, 360, 185
- Berry, R. & Burnell, J. 2000, *The Handbook of Astronomical Image Processing*, 1st edn. (P.O. Box 35025, Richmond, Virginia 23235, USA: Willmann-Bell, Inc.)
- Brown, T. M., Tumlinson, J., Geha, M., et al. 2013, *ArXiv e-prints*
- Calamida, A., Bono, G., Stetson, P. B., et al. 2007, *ApJ*, 670, 400
- Caldwell, N., Armandroff, T. E., Seitzer, P., & Da Costa, G. S. 1992, *AJ*, 103, 840
- Collins, M. L. M., Chapman, S. C., Rich, R. M., et al. 2014, *ApJ*, 783, 7
- Demers, S. & Harris, W. E. 1983, *AJ*, 88, 329
- Faber, S. M. & Gallagher, J. S. 1979, *ARAA*, 17, 135
- Faria, D., Feltzing, S., Lundström, I., et al. 2007, *A&A*, 465, 357
- Frank, M. J., Koch, A., Feltzing, S., et al. 2015, *A&A*, 581, A72
- Gallagher, III, J. S. & Wyse, R. F. G. 1994, *PASP*, 106, 1225
- Grebel, E. K. 2004, *Origin and Evolution of the Elements*, 234
- Harbeck, D., Grebel, E. K., Holtzman, J., et al. 2001, *AJ*, 122, 3092
- Harrington, R. G. & Wilson, A. G. 1950, *PASP*, 62, 118
- Hauck, B. & Mermilliod, M. 1998, *AApS*, 129, 431

- Howell, S. B. 2000, *Handbook of CCD Astronomy*, 1st edn. (The Edinburgh Building, Cambridge CB2 8RU, UK: Cambridge University Press)
- Hubble, E. P. 1925, *The Observatory*, 48, 139
- Irwin, M. & Hatzidimitriou, D. 1995, *MNRAS*, 277, 1354
- Kirby, E. N., Guhathakurta, P., Simon, J. D., et al. 2010, *ApJS*, 191, 352
- Kirby, E. N., Lanfranchi, G. A., Simon, J. D., Cohen, J. G., & Guhathakurta, P. 2011, *ApJ*, 727, 78
- Koch, A., Grebel, E. K., Kleyna, J. T., et al. 2007, *AJ*, 133, 270
- Koleva, M., de Rijcke, S., Prugniel, P., Zeilinger, W. W., & Michielsen, D. 2009, *MNRAS*, 396, 2133
- Komiyama, Y., Doi, M., Furusawa, H., et al. 2007, *AJ*, 134, 835
- Koposov, S. E., Belokurov, V., Torrealba, G., & Evans, N. W. 2015, *ApJ*, 805, 130
- Marigo, P., Girardi, L., Bressan, A., et al. 2017, *ApJ*, 835, 77
- Mateo, M. L. 1998, *ARAA*, 36, 435
- McConnachie, A. W. 2012, *AJ*, 144, 4
- Mighell, K. J. & Rich, R. M. 1996, *AJ*, 111, 777
- Peebles, P. J. E. & Yu, J. T. 1970, *ApJ*, 162, 815
- Prialnik, D. 2000, *An Introduction to the Theory of Stellar Structure and Evolution*, 2nd edn. (The Edinburgh Building, Cambridge CB2 8RU, UK: Cambridge University Press)
- Revaz, Y., Jablonka, P., Sawala, T., et al. 2009, *A&A*, 501, 189
- Ricotti, M. & Gnedin, N. Y. 2005, *ApJ*, 629, 259
- Riess, A. G., Filippenko, A. V., Challis, P., et al. 1998, *AJ*, 116, 1009
- Salvadori, S., Ferrara, A., & Schneider, R. 2008, *MNRAS*, 386, 348
- Schlafly, E. F. & Finkbeiner, D. P. 2011, *ApJ*, 737, 103
- Schuster, W. J. & Nissen, P. E. 1988, *AApS*, 73, 225

-
- Searle, L. & Zinn, R. 1978, *ApJ*, 225, 357
- Shetrone, M. D., Siegel, M. H., Cook, D. O., & Bosler, T. 2009, *AJ*, 137, 62
- Siegel, M. H. & Majewski, S. R. 2000, *AJ*, 120, 284
- Simon, J. D. & Geha, M. 2007, *ApJ*, 670, 313
- Spencer, M. E., Mateo, M., Walker, M. G., & Olszewski, E. W. 2017, *APJ*, 836, 202
- Strigari, L. E., Bullock, J. S., Kaplinghat, M., et al. 2008, *Nat*, 454, 1096
- Strömgren, B. 1963, *QJRAS*, 4, 8
- van den Bergh, S. 2008, *MNRAS*, 385, L20
- Vanhollebeke, E., Groenewegen, M. A. T., & Girardi, L. 2009, *A&A*, 498, 95
- Willman, B. 2010, *Advances in Astronomy*, 2010, 21
- York, D. G., Adelman, J., Anderson, Jr., J. E., et al. 2000, *AJ*, 120, 1579

Appendix A

Tables

Table A.1. Standard stars from Schuster & Nissen (1988), except HD 233511, HD 107583, HD 107853, HD 131653 and Hip 51769 from Hauck & Mermilliod (1998).

HD	Hip	y	$(b - y)$	m_1	c_1
33449	24037	8.488	0.423	0.201	0.273
43745	29843	6.062	0.355	0.192	0.418
44286	30167	6.752	0.159	0.169	0.842
46341	31188	8.616	0.366	0.145	0.248
51754	33582	9.000	0.375	0.144	0.290
56274	35139	7.750	0.384	0.157	0.273
62549	37752	7.723	0.385	0.182	0.375
64090	38541	8.279	0.428	0.110	0.126
75530	43393	9.167	0.443	0.254	0.257
81408	46191	9.610	0.560	0.478	0.210
88371	49942	8.414	0.407	0.186	0.329
94028	53070	8.225	0.343	0.078	0.251
107583	...	9.299	0.376	0.187	0.316
107853	...	9.095	0.320	0.157	0.475
108754	60956	9.006	0.435	0.217	0.254
118659	66509	8.827	0.422	0.196	0.244
123265	68936	8.348	0.504	0.356	0.348
131653	72998	9.510	0.442	0.225	0.252
132475	73385	8.555	0.401	0.063	0.285
134088	74067	7.992	0.392	0.137	0.255
134439	74235	9.058	0.484	0.224	0.165
134440	74234	9.419	0.524	0.297	0.173
137303	75542	8.774	0.611	0.610	0.178
138648	76203	8.137	0.504	0.358	0.290
142575	77946	8.608	0.274	0.101	0.545
149996	81461	8.495	0.396	0.164	0.305
159482	86013	8.387	0.382	0.126	0.277
233511	40778	9.716	0.339	0.071	0.258
G009-016	42887	9.317	0.237	0.103	0.489
G009-031	43595	10.823	0.398	0.158	0.224
G009-036	44033	11.934	0.381	0.124	0.195
G013-009	59109	9.998	0.311	0.048	0.373
G014-024	...	12.822	0.509	0.123	0.094
G014-039	...	12.828	0.587	0.267	0.153
G014-045	64965	10.803	0.587	0.517	0.115
G020-015	87062	10.591	0.452	0.032	0.247
G055-044	53169	9.765	0.606	0.555	0.152
G063-026	65418	12.183	0.328	0.085	0.277
G114-025	44111	10.654	0.296	0.155	0.422
G165-039	68321	10.069	0.309	0.056	0.359

Table A.1 (cont'd)

HD	Hip	y	$(b - y)$	m_1	c_1
G176-053	57450	9.912	0.397	0.100	0.180
W5793	43099	10.230	0.229	0.094	0.490
W8296	69232	10.685	0.415	0.098	0.183
...	47961	9.439	0.426	0.256	0.221
...	51127	9.734	0.568	0.461	0.182
...	51769	10.479	0.425	0.202	0.206
...	55805	10.394	0.377	0.131	0.220
...	74555	9.796	0.667	0.594	0.137
...	81294	10.332	0.565	0.469	0.192

Table A.2. Coefficients for Eq. (2.1).

Night	k_v	z_v	a_v	α_v	ρ_{zk}
28 February 2003	-0.294 ± 0.003	24.053 ± 0.004	0.023 ± 0.008	-0.037 ± 0.012	-0.996
1 March 2003	-0.292 ± 0.003	23.99 ± 0.004	0.03 ± 0.009	-0.002 ± 0.015	-0.998
2 March 2003	-0.287 ± 0.001	23.926 ± 0.002	0.037 ± 0.004	0.032 ± 0.009	-0.999
Night	k_b	z_b	a_b	α_b	ρ_{zk}
28 February 2003	-0.187 ± 0.007	24.145 ± 0.009	-0.003 ± 0.005	-0.087 ± 0.018	-0.979
1 March 2003	-0.18 ± 0.007	24.04 ± 0.009	-0.013 ± 0.007	-0.018 ± 0.023	-0.988
2 March 2003	-0.173 ± 0.002	23.935 ± 0.003	-0.015 ± 0.005	0.05 ± 0.014	-0.997
Night	k_y	z_y	a_y	α_y	ρ_{zk}
28 February 2003	-0.148 ± 0.005	24.261 ± 0.006	-0.005 ± 0.007	-0.18 ± 0.012	-0.994
1 March 2003	-0.135 ± 0.005	24.075 ± 0.007	-0.003 ± 0.008	-0.076 ± 0.016	-0.991
2 March 2003	-0.122 ± 0.002	23.888 ± 0.003	-0.001 ± 0.004	0.029 ± 0.011	-0.988

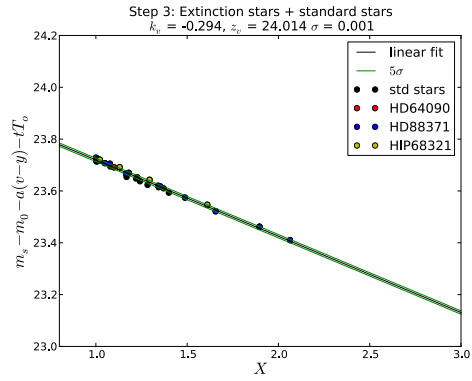
Note. — Constants for 1 March calculated as average between those of 28 February and 2 March because standard star observations are lacking for this night.

Table A.3. Excerpt from table of magnitudes and metallicities for stars in the direction of Leo II. For access to the full table, contact Sofia Feltzing at sofia@astro.lu.se.

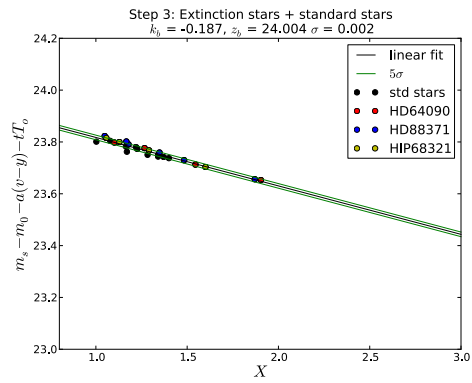
ID	RA (h)	Decl. (°)	v	ϵ_v	b	ϵ_b	y	ϵ_y	[Fe/H]	$\epsilon_{[\text{Fe}/\text{H}]}$
820	11:22318703	22.10500389	21.672	0.023	20.95	0.014	20.255	0.011	-2.979	0.051
1005	11:22319767	22.10713164	21.597	0.023	20.743	0.014	19.489	0.009	-4.851	0.051
1008	11:22311336	22.10718436	22.98	0.058	22.034	0.027	20.94	0.017	-3.849	0.042
1110	11:22319378	22.10828706	23.676	0.107	22.545	0.041	21.398	0.027	-3.282	0.032
1125	11:22531097	22.10850464	21.377	0.018	20.138	0.01	19.17	0.007	-2.184	0.026

Appendix B

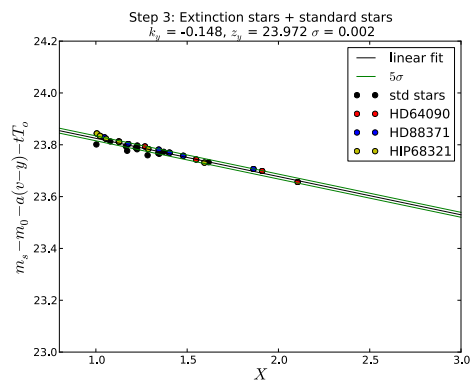
Plots



(a)

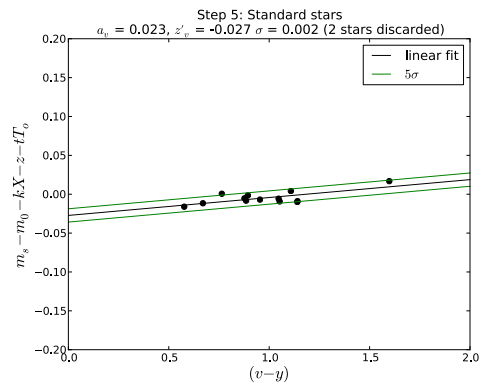


(b)

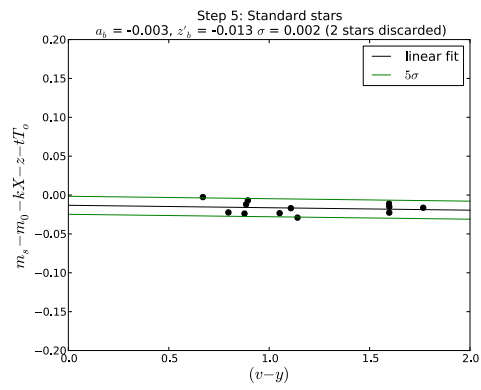


(c)

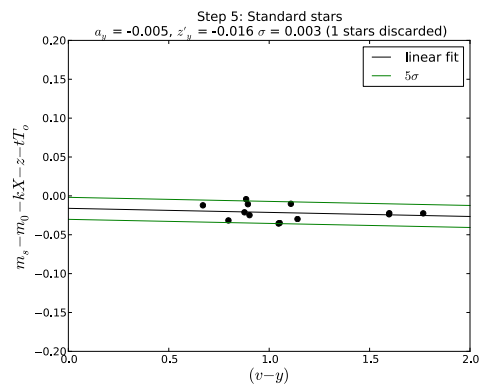
Figure B.1 Fit of airmass coefficient k and zero-point z for filters (a) v , (b) b and (c) y .



(a)

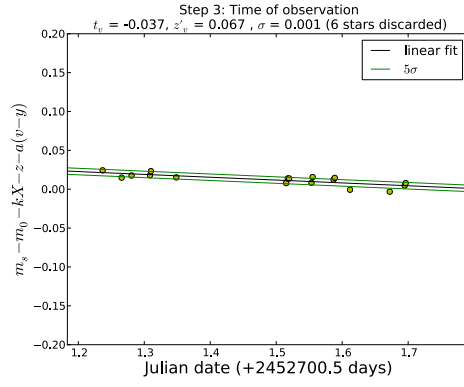


(b)

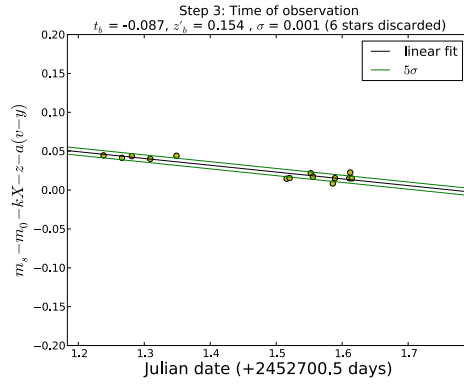


(c)

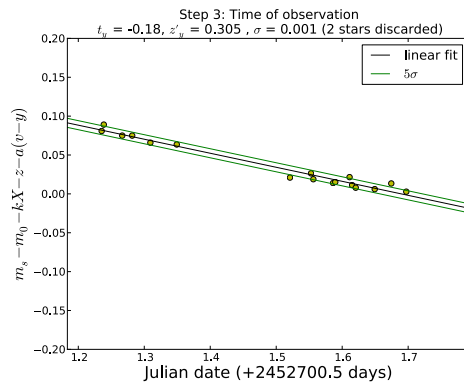
Figure B.2 Fit of colour coefficient a for filters (a) v , (b) b and (c) y .



(a)

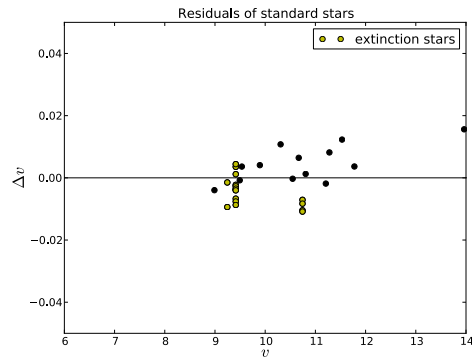


(b)

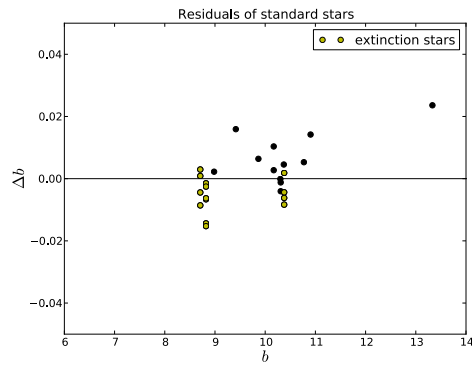


(c)

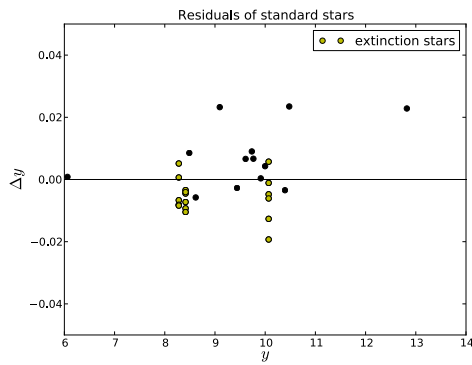
Figure B.3 Fit of time coefficient t for filters (a) v , (b) b and (c) y .



(a)



(b)



(c)

Figure B.4 Standard star residuals after applied airmass, colour, time and zero-point correction in filters (a) v , (b) b and (c) y .